Bio-hybrid soft robots with self-stimulating skeletons

Authors

Maria Guix[1]†*, Rafael Mestre[1]†, Tania Patiño[1,2], Marco De Corato[1], Judith Fuentes,[1] Giulia Zarpellon[1], Samuel Sánchez[1,3]*

Affiliations

[1] Institute for Bioengineering of Catalonia (IBEC), The Barcelona Institute of Science and Technology (BIST). Baldiri-Reixac 10-12, 08028 Barcelona, Spain.

[2] Chemistry Department, University of Rome, Tor Vergata, Via della Ricerca Scientifica, 00133 Rome, Italy.

[3] Institució Catalana de Recerca i Estudis Avançats (ICREA). Passeig de Lluís Companys 23, 08010 Barcelona, Spain

* Corresponding author
† These authors contributed equally to this work

Abstract

Bioinspired hybrid soft robots combining living actuation and synthetic components are an emerging field in the development of advanced actuators and other robotic platforms (i.e. swimmers, crawlers, walkers). The integration of biological components offers unique properties (e.g. adaptability, response to external stimuli) that artificial materials cannot replicate with accuracy, being skeletal and cardiac muscle cells the preferred candidates for providing contractile actuation. Here, we present a skeletal-muscle-based swimming biobot with a 3D-printed serpentine spring skeleton that provides mechanical integrity and self-stimulation during the cell maturation process. The restoring force inherent to the spring system allows a dynamic skeleton compliance upon spontaneous muscle contraction, leading to a novel cyclic mechanical stimulation process that improves the muscle force output without external stimuli. Optimization of the 3D-printed

skeletons is carried out by studying the geometrical stiffnesses of different designs *via* finite element analysis. Upon electrical actuation of the muscle tissue, two types of motion mechanisms are experimentally observed: i) directional swimming when the biobot is at the liquid-air interface and ii) coasting motion when it is near the bottom surface. The integrated compliant skeleton provides both the mechanical self-stimulation and the required asymmetry for directional motion, displaying its maximum velocity at 5 Hz (800 micrometer second^{-1}, 3 body length second^{-1}). This skeletal muscle-based bio-hybrid swimmer attains speeds comparable to cardiac-based bio-hybrid robots and outperforms other muscle-based swimmers. The integration of serpentine-like structures in hybrid robotic systems allows self-stimulation processes that could lead to higher force outputs in current and future biomimetic robotic platforms.

Summary

Skeletal muscle-based biobot with a self-stimulating serpentine spring skeleton presents inertial swimming with superior speed performance.

MAIN TEXT

Introduction

Biological systems have evolved throughout millennia to develop sophisticated mechanisms of self-organization (*1*), actuation (*2*), self-healing (*3*), and sensing (*4*). The robotics field aims to mimic and incorporate these complex behaviours (*5–8*). In the field of biomimetic soft robots, recent developments in material science enabled the fabrication of systems able to perform some simple types of actuation (*9*), including crawling (*10, 11*) or grasping (*12*), but they are still far from the degree of complexity, sophistication, and potential scalability toward small dimensions of their biological counterparts. One of the most investigated applications in soft

robotics is the development of artificial muscles that can mimic the performance of native muscle tissue (*13*, *14*). However, materials of synthetic origin still lack the ability to fully replicate the complexity and force output arising from the hierarchical organization of muscle tissue. To address the challenges of achieving the inherent mechanical properties (i.e. compliance, flexibility) and sensing capabilities from the native muscle, bio-hybrid robotics proposes a synergistic strategy to integrate the best characteristics of biological entities (i.e. self-healing, adaptability, sensing) and artificial materials for obtaining more efficient and complex systems (*15*, *16*).

Bio-hybrid robots, or biobots, are generally composed of muscle tissue, either cardiac or skeletal, and an artificial scaffold. In the last two decades, many of the fabricated biobots have been based on thin film structures (i.e. MEMS, PDMS and other elastomeric or non-elastomeric materials) seeded with cardiac or skeletal muscle cells (*17–27*), promoting a two-dimensional layer configuration that has been extensively explored for fish-like swimming purposes (*28*, *29*). Some examples include a swimming bio-hybrid soft robotic stingray based on optogenetically modified cardiac cells (*30*) or a cardiac-based medusoid that mimics the thrusting mechanism of a jellyfish (*31*). However, recent advances in both 3D printing (*32*) and tissue engineering (*33*) have allowed the creation of on-demand three-dimensional biological structures, instead of relying on 2D layer configurations, paving the way to their integration in smart soft robotic platforms.

Skeletal-muscle-based biobots actuation rely mostly on actuators or walkers (*34*, *35*). Some of the earliest skeletal muscle bio-hybrid systems were tethered and owed its actuation to the deflection of cantilevers by the muscle tissue (*36–40*) and used as grippers (*34*, *41*). However, in untethered bio-hybrid robots, crawling has been the main described motion mechanism (*42*). Additionally, while cardiac cells present spontaneous contractions whose response can be stimulated and synchronized at a certain frequency but cannot be stopped, skeletal muscle tissue possesses a wider range of adaptability and controllability, since these cells adopt a three-

dimensional structure that can be accommodated to different substrates and their contractions are induced on demand by means of an external electrical or optical stimulus (*43*, *44*). In addition, self-healing (*45*), adaptability (*44*), integration of motor neurons for advanced stimulation (*46*), long-time preservation (*47*, *48*), scalability (*49*) or their integration with micro-electrodes (*50*) were also demonstrated for skeletal-muscle bio-hybrid robots. The integration of neuronal and skeletal muscle tissue in one single biobot has been of great interest, as it resembles the structure of native muscle to obtain improved controllability of the bio-robotic systems (*51*, *52*). In this regard, a bio-hybrid swimmer with functional neuro-muscular junction that swims with time-irreversible flagellar dynamics has recently been reported (*53*). This biobot configuration represents the first swimmer based on skeletal muscle tissue, whose actuation relies on external light stimuli and it presents slow swimming speeds (0.92 µm/s) when moving at low Reynolds number regime.

Although several aspects concerning skeletal muscle based biobots controllability and scalability had been explored, it is key to find alternative efficient motion mechanisms and high force outputs to develop faster and more dynamic robotic designs. Here, we report a skeletal muscle-based swimming biobot with enhanced force performance and directional motion. The integration of a serpentine spring skeleton into the biobot platform allows proper mechanical integrity of the whole system, as well as mechanical self-stimulation due to the spring restoring force when spontaneous contractions take place during the cell maturation process. Such self-training event leads to enhanced actuation and larger contraction force in the biobot performance. This biobot is based on a three-dimensional skeletal muscle structure instead of 2D thin films as used in previous cardiomyocyte- and skeletal-muscle-based biohybrid swimmers mentioned above, offering a wider range of customization and actuation modes. Furthermore, the 3D serpentine spring structure that forms the compliant skeleton has been designed to present asymmetric stiffness throughout its structure, leading to a well-controlled bending of the biobot that permits

two different motion modalities: (i) swimming when located at the air-liquid interface, and (ii) coasting when it is placed near the bottom surface. Corresponding motion mechanisms were established by motion tracking and simulations of the locomotion hydrodynamics, revealing that the asymmetry in geometrical stiffness provides directional motion for the swimming case. In fact, our biobot design is the fastest skeletal muscle-based swimming bio-hybrid robot up to date by several orders of magnitude (791x, **Table 1**) and its velocity compares favourably with the bio-robotic systems based on cardiac cells. The integration of a serpentine spring on a bio-robotic platform serves both as a compliant skeleton useful for mechanical self-stimulation purposes and to provide asymmetry to the system. The versatility of 3D printing techniques, allowing for rapid and cost-efficient fabrication, added to the properties of this simple yet efficient flexible serpentine spring system demonstrates its potential for a better differentiation and performance of contractile cell-actuated robotic devices, inspiring future bio-hybrid robotic designs with higher efficiency and able to achieve more complex motion patterns.

Results

Skeletal muscle-based biobots with an integrated spring-like skeleton were constructed by assembling a cell-laden circular hydrogel around the compliant skeleton (**Fig. 1A**). The skeleton was composed of PDMS and created by extrusion-based 3D printing (**Fig. 1B**). The use of the 3D printing technique provided high versatility and fast prototyping, allowing the design and optimization of different configurations of the artificial skeleton. The main configurations considered were a symmetric (**Fig. 1C1**) and an asymmetric (**Fig. 1C2**) design, the latter including a small post bulging out of one of the sides. This element induced an asymmetric compaction of the skeleton of the biobot, necessary to achieve directional motion. The overall stiffness of the skeleton was tuned by varying the curing agent-to-base ratio of PDMS, but also an extra level of optimization was assessed by modifying its geometrical stiffness. Therefore, different serpentine designs in the central part of the biobot skeleton were considered and further evaluated (**Fig. 1C3**).

A rounded notch was included at both ends of the skeleton, being carefully designed and 3D-printed (**Fig. 1C4**) to hold the tissue ring in place and avoid its release during the maturation process or their motion evaluation. Finally, further optimization could be achieved by including different numbers of coils in the design to create biobots with different properties and sizes (**Fig. 1C5**). While the shorter skeleton design did not provide enough flexibility to the system, the design with higher number of coils led to a non-stable assembly of the scaffold to the skeleton due to its large bending at earlier stages. The optimal two-coil configuration, however, allowed an optimal balance between the restoring force and the biobot stability during the maturation process and later motion studies.

Regarding the active biological muscle-based actuator, the cell-laden scaffold was prepared by using customized 3D-printed molds with the desired circular shape and size. A hydrogel composed of fibrinogen, thrombin and Matrigel® and laded with skeletal muscle myoblasts was casted inside the mold (**Fig. 1D**), leaving the whole setup first in growth medium (GM) to let the cells grow and expand, and later on in differentiation medium (DM) to allow the differentiation process (*42*). Both GM and DM were supplemented with 6-aminocaproic acid (ACA) to reduce the degradation of the hydrogel due to proteases (*47*). The cross-linking of the hydrogel was studied over time to closely evaluate the gelation process and obtain reproducible cell-laden scaffolds for the biobots construction. **Fig. 1D** shows the shear storage and loss moduli of the hydrogel at 37 °C at a frequency of 1 Hz for 90 min. At the start of the characterization, when fibrinogen, thrombin and Matrigel® have been mixed, an initial peak in both moduli after 5 min points at the fast cross-linking of fibrinogen into fibrin by the action of the enzyme thrombin. After approximately 30 min at physiological temperatures, another increase in the absolute value of the shear modulus indicates the thermal-induced cross-linking of Matrigel®. After this point, the structure of the cell-laden hydrogel is stable and warm GM can be added to the injection mold for cell culture.
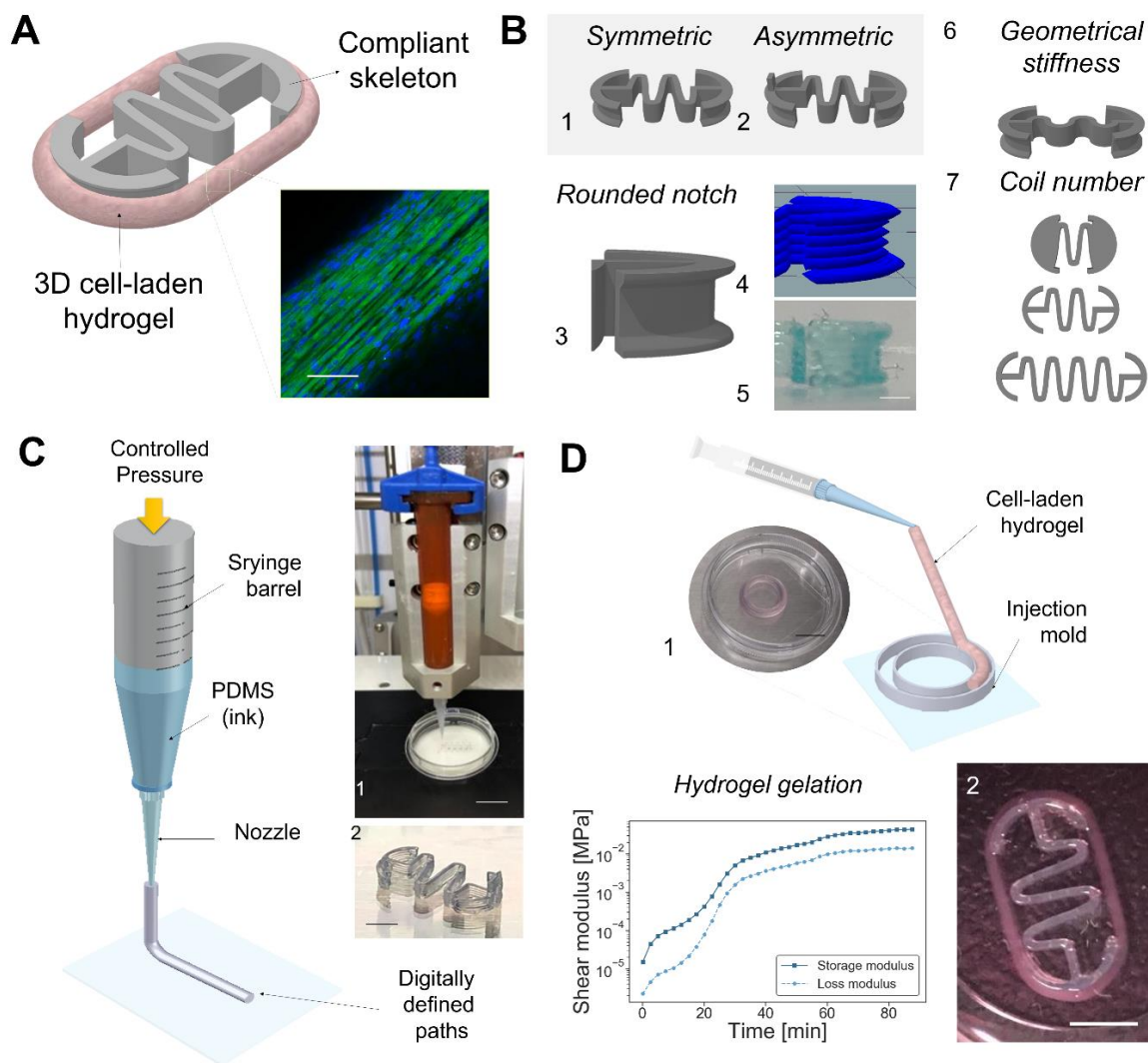
Fig. 1. Biobot design and fabrication. (**A**) Schematic of a biobot consisting of a skeletal muscle cell-laden hydrogel acting as a bio-actuator (CLSM image of aligned skeletal muscle cells) assembled to a compliant spring-like PDMS skeleton. Scale, 100 µm. (**B**) 3D printing process based on direct ink writing, where the hydrogel (PDMS) is printed onto a flat surface (1) to obtain the biobot compliant skeleton (image in (2)). Scale bar, 1 cm in (1) and 3 mm in (2). (**C**) Different designs of the compliant skeleton, based on a (1) symmetric or (2) asymmetric serpentine flexure with a (3) rounded notch for a perfect assembly of the cell-laden hydrogel (the (4) 3D visualization of layer-by-layer view of the G-code instructions and (5) image of a printed notch). The effect of (6) different angles on the geometrical stiffness and (7) coil numbers were explored to modulate the mechanical properties of the compliant skeleton design. Scale, 1 mm (**D**) The fabrication

process of 3D cell-laden molds (image of a mold (1)) and characterization of (2) mechanical properties related to the of the cell-laden hydrogel cross-linking, as well as a real image of a self-assembled biobot. Scale bar, 3 mm.

The preparation and maturation process of the skeletal muscle biobot comprises several stages. **Fig. 2** depicts the process timeline to obtain a myoblast-laden hydrogel. In stage 1, C2C12 cells are embedded in the 3D scaffold and left to grow for three days, leading to a myoblast-laden hydrogel. The hydrogel composition was adapted from Raman et al. (*42*), using a 4 mg/mL fibrinogen and 30% (v/v) Matrigel concentration, which has been reported to be the ideal concentrations for optimal muscle performance (*54*). The cell-laden scaffold is manually transferred to the 3D-printed compliant skeleton based on PDMS in presence of DM (Stage 2). At this point, insulin-like growth factor (IGF-1) present in solution promotes the fusion and differentiation of myoblast into myotubes (*35*), supporting the differentiation process and leading to the natural compaction of the muscle-actuator around the compliant skeleton. During the maturation process, the cell-laden scaffold will perfectly adapt to the skeleton's shape thanks to the rounded edges, avoiding the formation of stresses that could damage the tissue. Due to these compaction forces and to the rounded notches that prevent disassembly, the biobot adopts a buckling structure that provides the necessary asymmetry to the biobots conformation for optimal motion (Stage 3).

The compliant mechanism of our untethered bio-hybrid robot is based on the longitudinal force exerted along the beam axis by the muscle tissue around the serpentine-like skeleton upon electrical pulse stimulation (EPS) (**Fig. 2B**). The compliant nature of the spring serpentine structure allows its deformation with low geometrical stiffness and a restoring force that brings the biobot back to its original state.
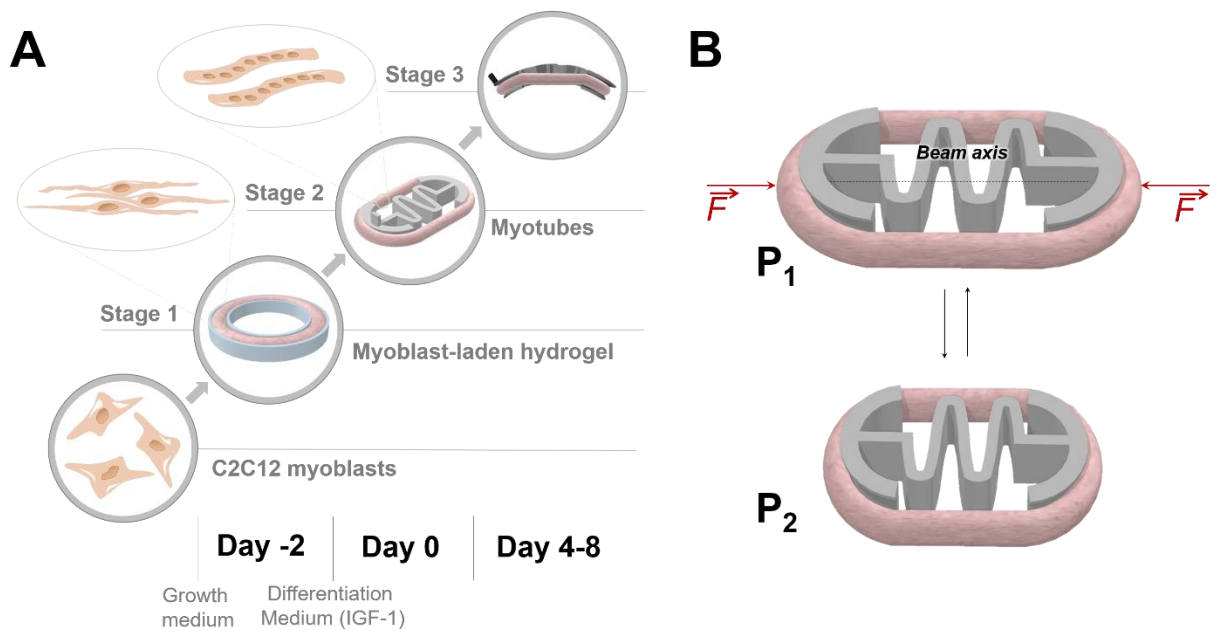
Fig. 2. Cell differentiation and compliant mechanism at the biobot platform. (**A**) Conceptual schematic of the cell maturation process at the biobot platform, along with the timeline in which cells seeding, mold preparation (Stage1), assembly (Stage 2), and bending (Stage 3) takes place. (**B**) Schematic representation of the compliant mechanism of the biobot, where compression (P2) and expansion state (P1) of the serpentine flexure are induced by the contraction forces of the muscle and spring-like relaxation behaviour of the assembled muscle cell-based bio-actuator upon EPS.

The skeleton optimal geometrical parameters were evaluated by using finite element analysis (FEA). To study the effect of the spring design on the compression efficiency, we designed three different geometries: i) case 1, with a low-degree variation along the serpentine, creating low amplitude oscillations; ii) case 2, with much larger amplitude in the oscillations, allowing a better distribution of the stresses; and iii) case 3, with large amplitude, but a strict 180° angle at the points of curvature (**Fig. 3A**). In order to mimic the compression from the skeletal muscle tissue contraction on the compliant skeleton, two uniaxial point forces of the same magnitude were applied at both sides of the structure in a 3D simulation (assuming static

conditions and only mechanical and linear deformations). The profile of a real twitch contraction was measured by image difference and were normalized in a way that the maximum value was 100 µN (more details in SI section) for a more meaningful simulation of the contraction kinetics. On the right side of **Fig. 3A**, we calculated the von Mises stresses of each skeleton case for a compression force of 100 µN. The von Mises stress is used to predict yielding of materials under complex loading from the results obtained from uniaxial tensile test and provide information about the equivalent stress distribution across the whole structure. The higher and localized stress values obtained for cases 2 and 3 already indicate that these structures can probably compress easier than case 1, although a better characterization of this can be obtained by calculating the geometrical stiffness of the designs.

The geometric stiffness of the skeletons is a parameter that gives information about the stiffness of the material after applying a deformation, taking only into consideration the geometry of the structure. For each design, we performed a force sweep using the contraction profile with a maximum force in the range of 10-100 µN (symmetrically at both edges), based on reported forces in the literature (*35*, *43*). The maximum uniaxial compression of the compliant skeleton, which coincided in time with the maximum force of the contraction profile, was plotted in terms of the force (left top side **Fig. 3A**), revealing a linear elastic response dictated by Hooke's law, that allowed us to calculate the geometrical stiffness of the material, *k*, by the equation $F = kx$, where F is the applied force and *x* the compression. The inverse of the slope yields the geometrical stiffnesses (left bottom side **Fig. 3A**), where we can see that case 1, with a soft curvature in its coil, had much larger geometrical stiffness than the other two cases, which presented slightly similar values. Further experiments with 3D-printed skeletons revealed that case 3 was easily compressible and collapsed, making the serpentine coils touch and stick to each other. Therefore, the design of case 2 provided the appropriate stiffness conditions for muscle-induced compression in the expected force ranges. However, the compliant structure stiffness can also be tuned by

changing the ratio of elastomer to curing agent (**Fig. 3B**). We explored the impact of the PDMS

chemical composition by preparing skeletons with the case 2 at different ratio of elastomer to

curing agent: 1:20 (red), 1:15 (green) and 1:10 (blue), ordered from less to more stiffness. As

expected, the compaction of the cell-laden hydrogel around a skeleton at 1:20 is higher than the

1:10, demonstrating the feasibility to tune the structural configuration of the biobot' skeleton by
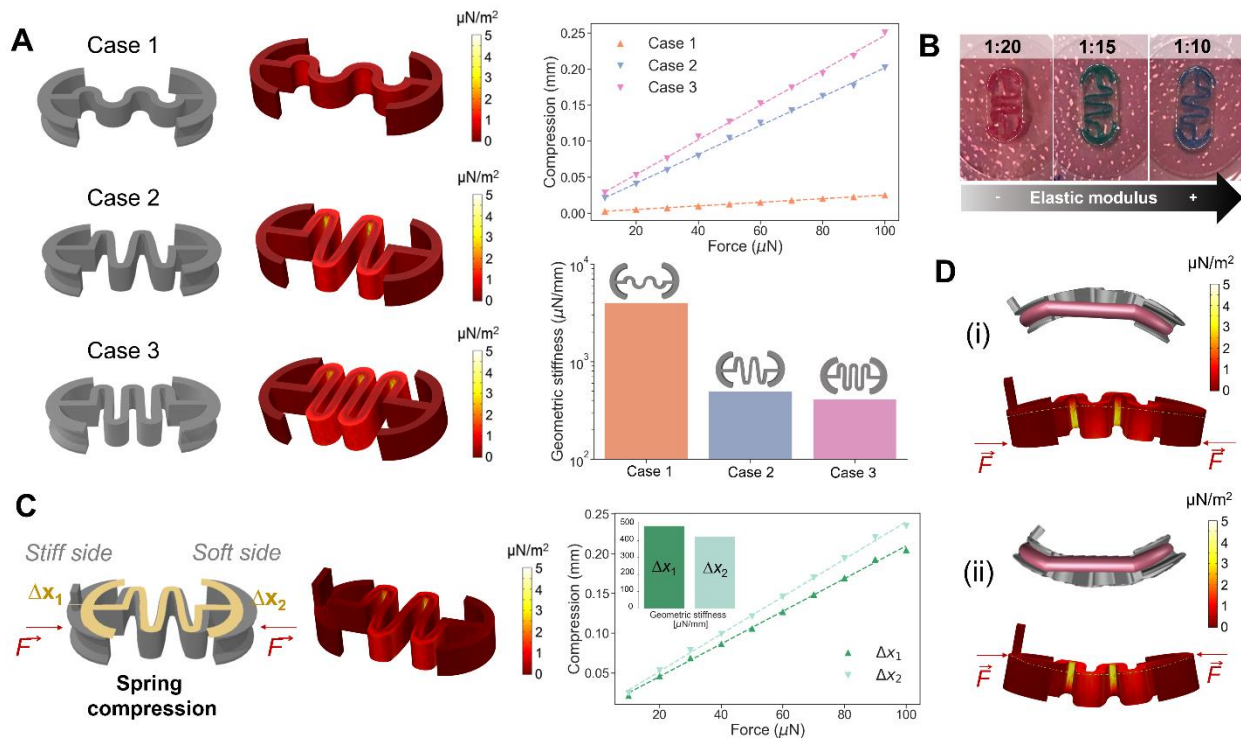
changing its mechanical stiffness.

Fig. 3. FEA simulations of mechanical deformation on biobot compliant skeleton. (**A**) Three

different cases were considered to optimize the coil curvature and shape, depending on the

geometrical stiffness of the construct. Next to the 3D representation of each case, the Mises

stresses of each structure after a symmetrical load of 100 µN on each side are presented. The

maximum compression of the skeleton in terms of the applied force (right top) and geometrical

stiffness (right bottom) were obtained per each of the three cases (**B**) Stiffness modulation

properties tuned by PDMS chemical composition; different coloured dyes were included to the

PDMS to differentiate them, corresponding red, green and blue to 1:20, 1:15 and 1:10,

respectively. (**C**) Stiffness evaluation in presence on an asymmetric skeleton. (**D**) Bending analysis

allow to study the buckling behaviour on the compliant skeleton, revealing that there is inhomogeneity in the compaction that can be related to buckling, which it can happen both towards the leg or the opposite direction.

Having defined optimal serpentine structure, the asymmetry of the bio-hybrid robot was also studied by FEA simulations (**Fig. 3C**). Likewise, by simulating two uniaxial equivalent contraction profiles at both sides of the skeleton, we observed that the presence of a small post bulging out of one of the sides induced a differential compression of the structure. In this compression *vs* force plot, it can be seen how the maximum compression of the stiffer side (with the induced asymmetry), termed Δx_1, was larger than the compression in the softer side, Δx_2, as demonstrated on the geometrical stiffness evaluation. Finally, we studied the feasibility of the buckling behaviour by inducing a uniaxial compression force at both sides of the skeleton, but out of center, as indicated by the force vectors in **Fig. 3D**. These forces mimicked the passive compaction of the tissue that occurs during myogenesis (*35*, *43*). We hypothesize that this effect could be caused by a spontaneous symmetry breaking during tissue compaction, probably due to a combination of the heterogeneity of the muscle constructs that could lead to an asymmetric distribution of the compression forces and the interaction with close interfaces. For robotics systems at small scales, symmetry breaking is key to achieve efficient motion (*55*). Therefore, we expect that this differential compression produces a difference in the fluid flow fields, leading to directional motion.

It is known that dynamic mechanical stimulation is beneficial for the differentiation and maturation of skeletal muscle cells, as it mimics the conditions of native tissue (*56*, *57*). Therefore, we hypothesized that the spring-like configuration of the serpentine skeleton provided dynamic stimulation after spontaneous contractions by reacting with an opposite restoring force that could further expand the tissue, offering mechanical stretching in the form of a feedback loop. To demonstrate this, we compared two types of biobots: i) the compliant and untethered spring-like

skeleton, and ii) a 2-post system that was tethered and less compliant (**Fig. 4A**). During myogenesis, we checked for the presence of spontaneous contractions *via* optical microscopy revealing that, after 4 days of differentiation (D4), only spring-like biobots were showing strong spontaneous contractions, fully synchronized and at a frequency of approximately 3 Hz, while bio-actuators in the 2-post system were not showing any spontaneous contractions (**Fig. 4B**). At D8 of differentiation, the muscle tissue in the 2-post system showed small, localized contractions that were not synchronized and, eventually, at D10, the spontaneous contractions were strong and globally distributed, as in the bio-hybrid robot (**Fig. 4B, Movie S1**).
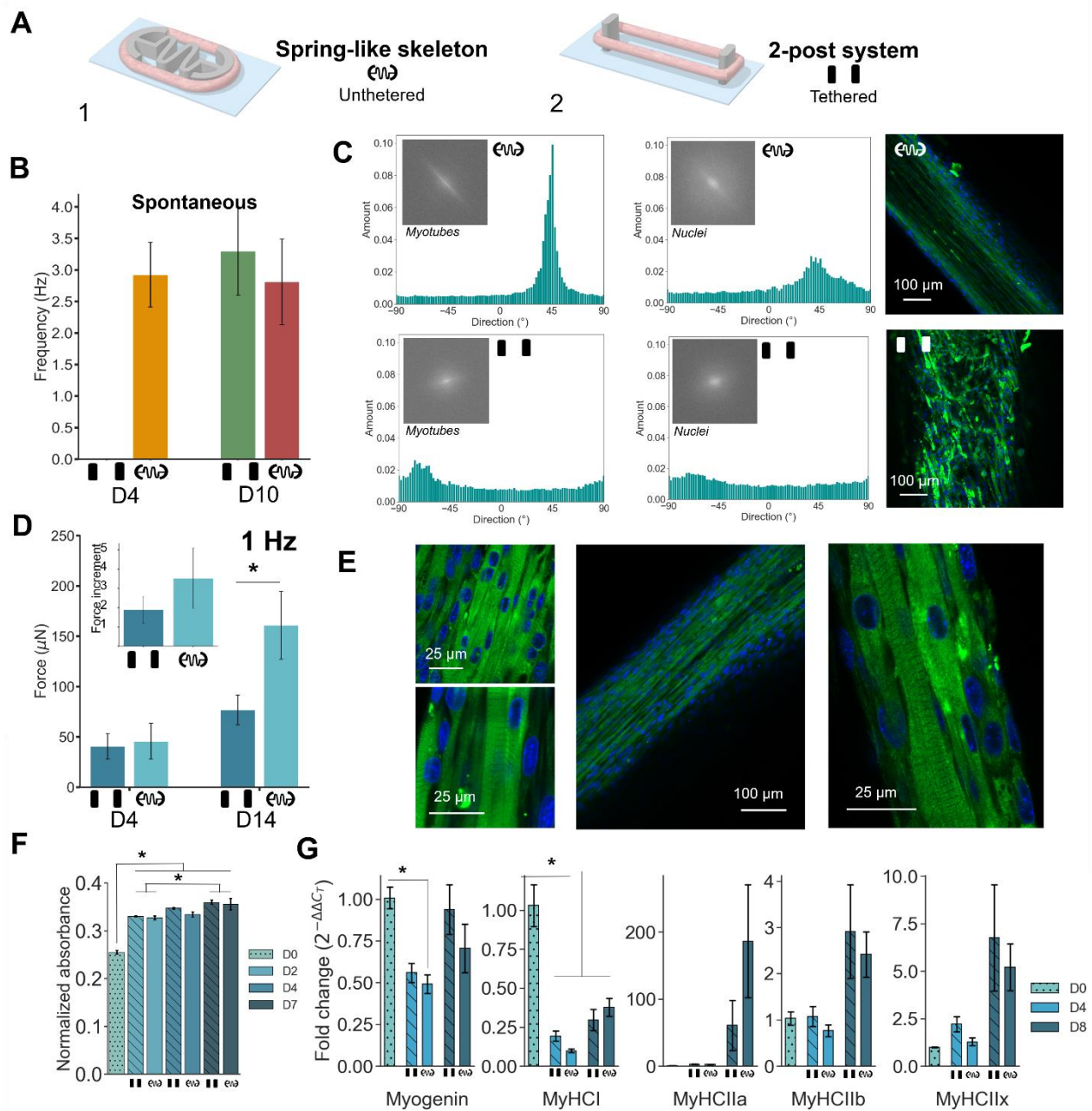
Fig. 4. Force generation and biological characterization of skeletal muscle biobots. (**A**) Schematic of spring-like skeleton setup (1) and 2-post system (2). (**B**) Spontaneous contraction evaluation at D4 and D10. N = 4-6. (**C**) Directionality histograms for the myotubes and nuclei structures when matured in the two-post system and the spring skeleton. (**D**) Force measurement of the 2-post system and biobot system at D4 and D14 of differentiation and force increment (inset). N = 3-4. * indicates significance difference (p-value < 0.05; Student's t-test). (**E**) Confocal evaluation of the tissue ring in a biobot showing the presence of sarcomeric structures. Myosin

Heavy Chain II: green; cell nuclei: blue. (**F**) PrestoBlue viability/metabolic activity assay showing

the normalized absorbance for samples at D0 of differentiation in the mold (dotted bar) and

differentiated in the 2-post (stripped) or spring-like (empty) systems. N = 3-4. * indicates

significance difference (p-value < 0.05; Tukey's HSD test). (**G**) RT-qPCR analysis for samples at

D0 in the mold (dotted bar) and differentiated into the 2-post (stripped) or spring-like (empty)

systems. N = 3. * indicates significance difference (p-value < 0.05; Tukey's HSD test). Error bars

in all figures represent standard error of the mean.

The movement index of the contractions, defined as the pixel difference between images in

a small region of interest (ROI) of the tissue, is shown in **Fig. S1A** at D4 of differentiation. It can

be seen how only the biobot in a spring-like skeleton showed periodic spikes in its movement

index (representing the spontaneous contractions), while the signal of the 2-post system was

mainly noise. A fast Fourier transform (FFT) of this signal (**Fig. S1B**) further confirmed that only

the former showed synchronized and defined contractions at 3 Hz, while the signal of the latter did

not have any defined frequencies and was just noise.

The alignment of the myotubes within the tissue constructs were studied by directionality

analysis using FFT of immunostaining images (**Fig. 4C** and **S2**). In the spring-like skeleton,

myotubes were highly aligned and nuclei also showed elongation towards the same direction.

However, in the 2-post system, this alignment was not so outstanding. We hypothesize that the

dynamic and compliant nature of the spring-like skeleton induces the alignment of the myotubes

due to the constant stretching supplied by spontaneous contractions and restoring force. The

strength of the contractions was also evaluated and compared (**Fig. 4D, Movie S2**). Although the

bio-actuator in the 2-post system did not present spontaneous contractions at D4, EPS could induce

contractions in the tissue, which were of a similar magnitude to those induced in the biobot.

However, force measurements after several days in differentiation demonstrated that the muscle

tissue of the spring-like biobot had increased its force almost 4-fold, while the 2-post bio-actuator only by 2-fold, which could be related to the improved alignment of the cells in the spring-like skeleton (**Fig. 4D**). Confocal immunostaining of myosin heavy chain II (MyHCII) and cell nuclei showed the presence of sarcomeric structures in the hybrid biobot (**Fig. 4E**).

Further biological characterizations were performed to elucidate the reason behind the force difference between tissues in the 2-post or the spring-like system. The diameter of myotubes differentiated in both systems were compared and yielded values between 13-14 µm without statistically significant differences between them, similar to previous reports in the literature (*21, 58*), therefore the force difference could not be due to hypertrophic myotubes (**Fig. S3**). Viability/metabolic activity assays showed a plateau after 2 days of differentiation (as the cells were not proliferating anymore), thus the tissues in the 2-post or spring-like systems were equally viable (**Fig. 4F**). Finally, real time quantitative polymerase chain reaction (RT-qPCR) of several maturation-related genes (myogenin, MyHCI, MyHCIIa, MyHCIIb and MyHCIIx) was performed at different timepoints (D0, D4 and D4) for both systems (notice that D0 coincide, since both samples were transferred to their scaffolds at that point). In general, we observed a downregulation of MyHCI and upregulation of the isoforms of MyHCII, as expected for skeletal muscle tissue during maturation, in a slow-to-fast myosin transition (*59, 60*). Although not statistically significant due to the high variability of the samples, MyHCIIa in average seemed to be upregulated in the spring-like skeleton compared to the 2-post system, which could be related to the stronger force output reported in **Fig. 4D**. In any case, given the same levels of myotube diameter, similar metabolic activity and comparable expression of myosin genes, the increased force generation of the spring-like biobots is likely to have its strongest contribution from the enhanced alignment and the restoring force feedback.

After at least 4 days of differentiation, the hybrid biobots could show a spontaneous symmetry breaking leading to a buckling structure, as depicted in **Fig. 2A** and validated in **Fig.**

3D. However, due to the hydrophobicity of PDMS and surface tension at the air-liquid interface, biobots with a symmetric skeleton remained floating without showing any buckling behaviour (**Fig. 5A1, Movie S3**). An asymmetry in the form of buckling was induced in the symmetrical skeletons by forcing the biobot inside the culture medium, while working in a plastic Petri dish, during the differentiation process. The presence of a notch at each skeleton's edge prevents the release of the cell-laden hydrogel when the bending of the bio-hybrid robot takes place. While the glass surface aids to a better assembly of the cell-laden hydrogel to the notch at the early maturation stages (from D0 to D5) by ensuring that the PDMS skeleton remains completely flat due to the hydrophobic interactions, the plastic surface presents different surface tension with a weaker interaction, allowing the desired buckling effect to achieve and efficient swimming motion.
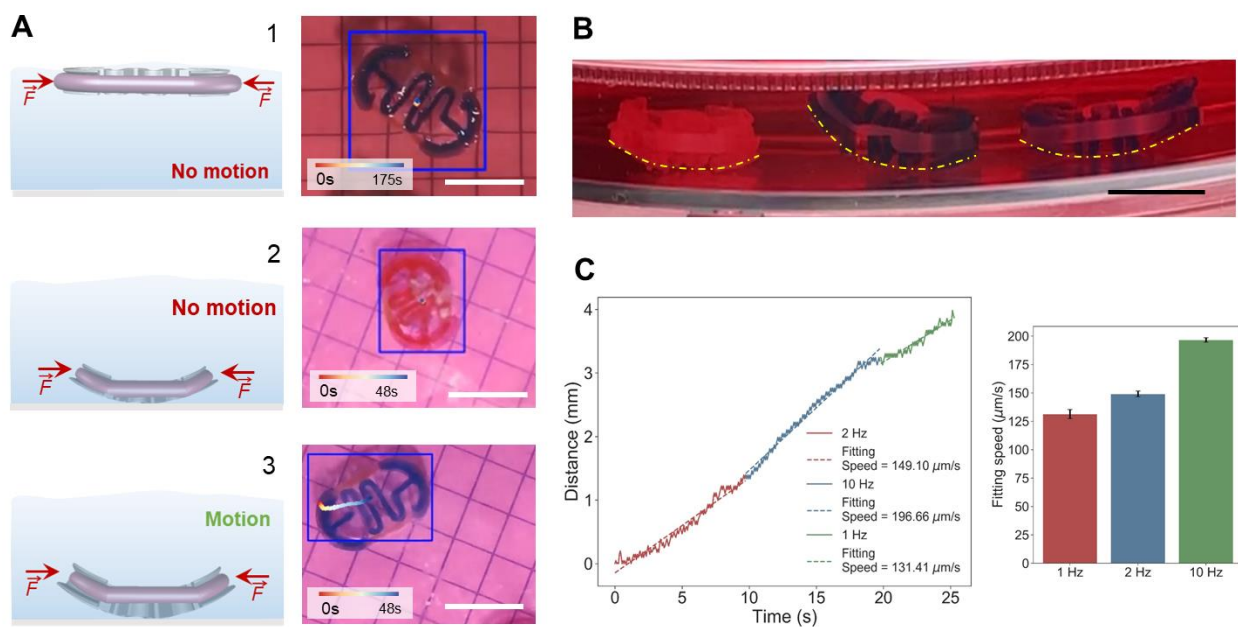

Fig. 5. Symmetric biobot motion evaluation. (**A**) Schematic of the side position and top image from the symmetric biobot when located at the interface (1), and in solution for the two cases where no motion (2) and motion (3) is taking place. Scale bar, 10 mm. (**B**) Side image of three different biobots with different stiffnesses, with the corresponding bending due to the buckling effect. Scale bar, 10 mm. (**C**) Speed analysis for the case of the symmetric biobot at different frequencies. Error bars represent the error of the least-squares fitting.

For the biobots with a symmetric skeleton, two different cases where studied. In the first one, considered the biobot, maintained at the air-liquid interface, no significant motion was observed (**Fig. 5A1**, **Movie S3**). However, when the symmetric biobot was placed near to the bottom surface, buckling deformation was spontaneously generated due to the heterogeneity of the muscle construct yielding a net compaction force outside its axis of symmetry (**Fig. 5A2 and 5A3**), observing motion for some of the symmetric biobot upon EPS. This spontaneous symmetry breaking and thus the degree of deformation could not be controlled, but it was dependent on the stiffness of the material, given by the curing-agent-to-base ratio of PDMS. In **Fig. 5B**, we can see that low stiffness PDMS (left) would completely compress and collapse the structure, while higher stiffnesses (medium and right) would allow some freedom of movement that could result in net motion. **Fig. 5C** shows an example of the displacement of the best-case scenario of symmetric swimming, which could reach maximum speeds of 100-200 µm/s (or 0.5-1 bl/min), increasing with frequency (**Movie S4**). This type of motion could resemble the swimming style of certain fish near surfaces, such as the burst-and-coast behaviour of zebrafishes, characterized by sporadic bursts followed by coasting phases (*61*, *62*). The strong hydrodynamic couplings between the flow field around the biobots and the bottom surface, which are known to play a substantial role in the motion of microorganisms (*63*), may also play a significant part in this case. For instance, it is known that hydrodynamic coupling induces the alignment of the swimming direction of a microorganism with the nearby surface (*63–66*). It should be considered, however, that the motion resulting from symmetric skeletons was not predictable, as it strongly depended on the degree of buckling curvature, which could not be controlled. Moreover, both the speed and the direction of motion were not clearly defined, as they relied on spontaneous symmetry breaking of the structure and its interactions with the surfaces. Therefore, consistent and controllable motion was only obtained when an asymmetry was previously incorporated in the design.

Motion with asymmetric skeletons proved to be predictable in terms of yield and direction of swimming. The presence of the post on one of the sides of the skeleton's design induced a different stiffness of the two sides of the skeletons, as previously demonstrated by FEA analysis in **Fig. 3C**, as well as allowing stable floating of the buckled structure, unlike in the case of the symmetric biobots that required to be placed to the bottom surface (**Fig. 6A**). In general, while symmetric designs moved only under certain conditions that broke its symmetry at speeds lower than 100 µm/s, asymmetric biobots swam at higher speeds and in a consistent manner (direction opposite to the post), although with great variability between samples (**Fig. 6B**). Moreover, the yield of biobots (defined as the percentage of biobots moving with respect to the full sample) was much higher for asymmetric skeletons (~60%) than for symmetric ones (~25%).
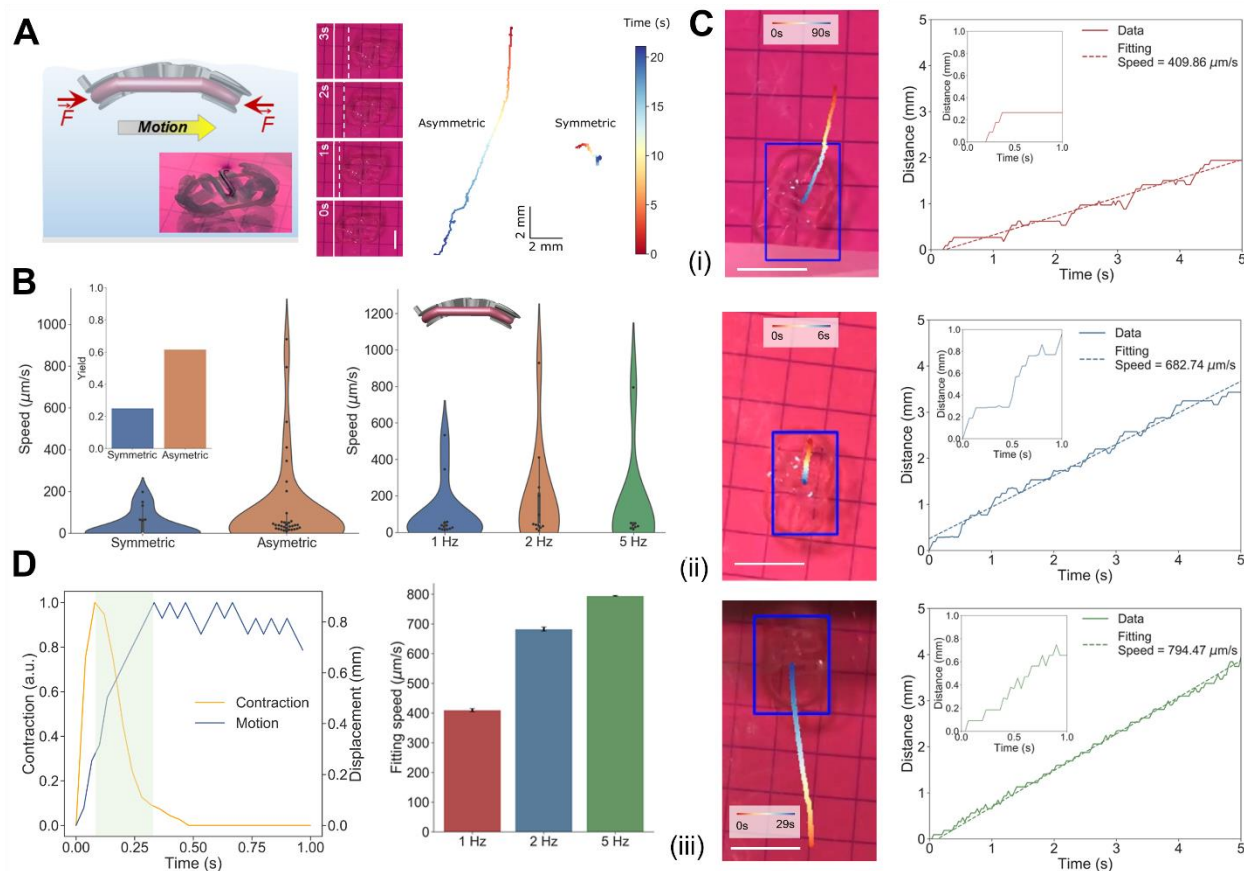

Fig. 6. Asymmetric biobot evaluation. (**A**) Schematic of the side position and time step image of an asymmetric biobot motion for 3 seconds and its corresponding speed under different EPS frequencies. On the right, sample trajectories of an asymmetric and symmetric biobot. (**B**) Violin

plots of the speed of symmetric *vs*. asymmetric biobots. Yield of moving biobots with respect to the total sample (inset). On the right, violin plots of the speed of asymmetric biobots for different frequencies. (**C**) Motion evaluation of the asymmetric biobot, depicting its motion efficiency with an image where the corresponding track is shown, as well as its displacement over time, at (i) 1 Hz, (ii) 2 Hz, and (iii) 5 Hz. Scale bar, 10 mm. (**D**) Superposition of a measured contraction (yellow) with the motion of a biobot after one contraction. The green-shadowed portion represents the region of motion that can only be explained by inertia. Average motion of asymmetric biobots upon different EPS frequencies. Error bars represent the error of the least-squares fitting.

Three tracking examples for the biobots with an asymmetric skeleton at different stimulation frequencies are also shown, where speeds of more than 700-800 µm/s for frequencies of 2 Hz and 10 Hz, and 550 µm/s for 1 Hz can be observed (**Fig. 6C**, **Movie S5**). In the insets of 1 Hz and 2 Hz, we can see how the motion occurs in a stepwise manner, while for 5 Hz it is more continuous. Comparing the average trajectories of both designs from all the trackings, we found that both symmetric and asymmetric biobots were able to achieve motion. An interesting common feature of asymmetric biobots is the stepwise motion, consistent with swimming mechanism driven by inertia (**Fig. 6D**). In fluid mechanics, the relationship between inertial forces and viscous forces during the motion of a swimmer is known as the Reynolds number (Re). This dimensionless quantity allows to differentiate between regimes of motion in which laminar flows (typical of viscous motion) or turbulent flows (typical of inertial motion) are dominant. At low Re ($\ll$ 1), where viscous forces dominate, the fluid dynamics are described by the time-independent Stokes equation, in which inertial components are considered negligible. At this scale, the "scallop theorem" by Purcell dictates that a swimmer must perform non-reciprocal or time-irreversible motion to achieve a net displacement different from zero (*67*). Microorganisms manage to break this time-reversal symmetry by rotatory motions (*68*), like those of bacterial flagella (*69*), which have been mimicked by artificial micropropellers (*70*) or bio-hybrid swimmers based on cardiac

cells (*71*). In our case, the compression mechanism of the skeletal muscle tissue against the skeleton is time-reversible since the shape changes are identical if time is reversed. This bio-swimmer, therefore, should not present motion at low Re. The Re number is defined as $Re = v\,L/v$, where v is the characteristic fluid velocity, L is the characteristic length of the swimmer and v the kinematic viscosity of the fluid. In our case, given an approximated size of 10 cm and speeds of the biobots between 100-500 µm/s, we find Re numbers of the order of 1-5. In this range, both viscosity and inertia play a significant role, and the motion cannot be considered neither purely viscous nor purely inertial.
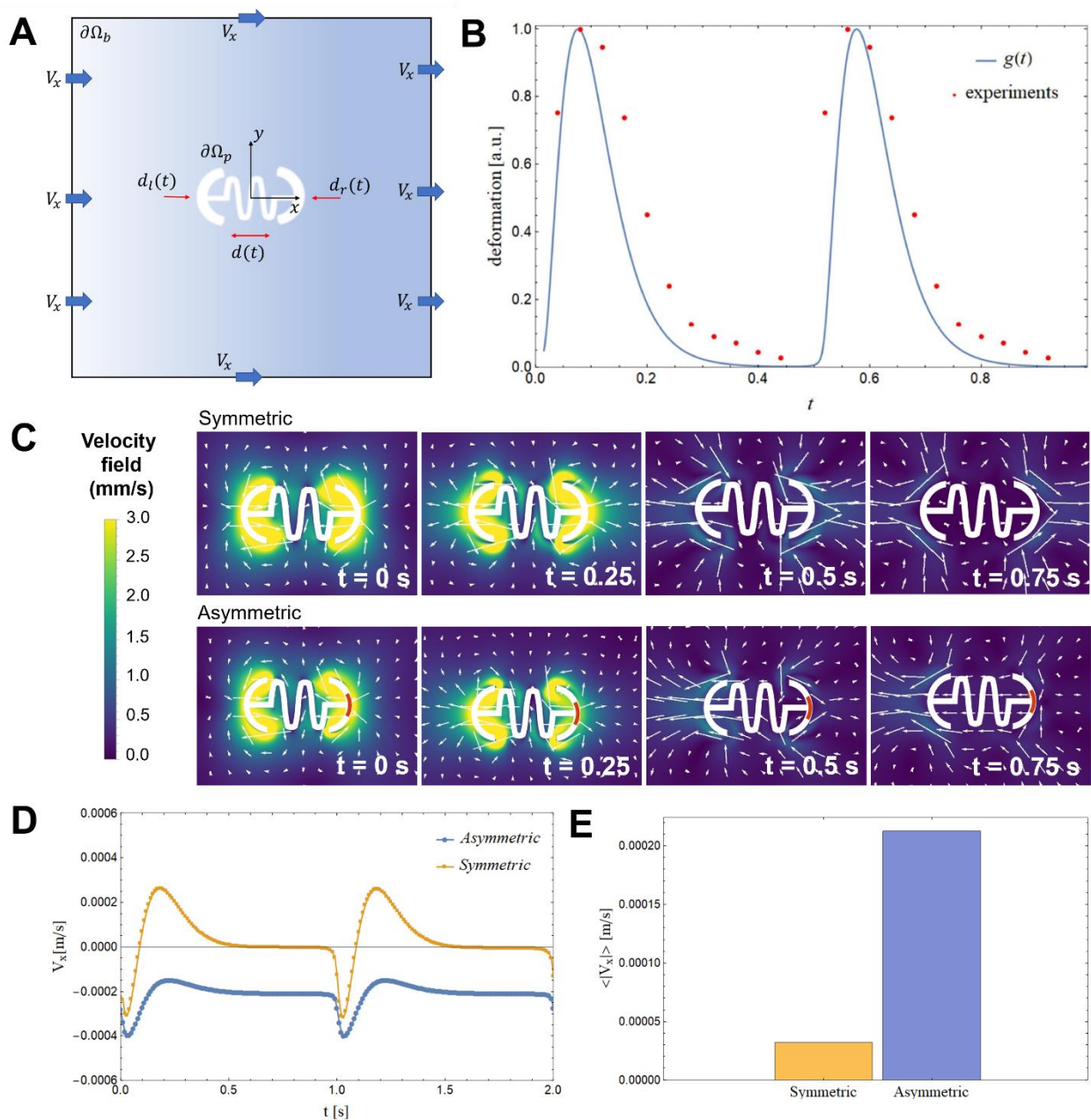
Fig. 7. Hydrodynamics of biobots locomotion. (**A**) Schematics of the 2D computational model.

(**B**) Periodic deformation of the biobot used in the simulation compared to that measured in the

experiments. (**C**) Magnitude of the velocity field and streamlines at four different instants during

one period, in the case of a biobot driven at 1Hz. The top panels show the result for a symmetric

biobot, the bottom panels show the results for an asymmetric biobot. The orange icon at the right

side of the biobot represents the region with the post (stiffer section experiencing smaller

deformations). (**D**) Evolution of the x component of the velocity of the biobot during two periods. (**E**) Average speed of the biobot over one period in the case of a stimulation at 1Hz.

Hydrodynamics simulations were performed to demonstrate that the fluid inertia and the asymmetric deformation of the biobot upon muscle contraction are key to its locomotion. Due to the high computational power of simulating the deformation of three-dimensional structures coupled with hydrodynamics, a 2D model was used instead (see SI). As shown schematically in **Fig. 7A**, we modelled the time-dependent deformation of the left side of the biobot as $d_l(t) = \Delta_l\, g(t)$, and of its right side as $d_r(t) = \Delta_r\, g(t)$. The deformation of the skeleton in the middle was set to vary linearly between these two values (see SI). The maximum compressions, Δ_l and Δ_r, were equal in the case of a symmetric biobot but different in the case of an asymmetric one with distinct geometric stiffness on each side. The periodic deformation of the skeleton due to the contraction and the relaxation of the muscle cells, $g(t)$, was chosen to closely follow the measured deformation in the experiments, as shown in **Fig. 7B.** This contraction profile is typical of skeletal muscle tissue, as it is known to go through a fast period of contraction followed by a slower relaxation (**Fig. 6D**) (*43*). Since the contraction and relaxation of the skeleton are time-reversible we expected propulsion only if Δ_l is different from Δ_r.

The snapshots in **Fig. 7C** show the magnitude of the velocity field and the streamlines around the biobot during one contraction/relaxation period as computed from the numerical simulations. In the top panels, displaying the symmetric case, the left and the right side of the biobot deformed in the same way $\Delta_r = \Delta_l$. As a result, the streamlines on the left and on the right of the biobot were highly symmetric and the net displacement of the biobot, averaged over one period, was negligible. This is confirmed by looking at **Fig. 7D** and **E**, which show the velocity of the symmetric biobot as a function of time and its average over one period.

In contrast, a biobot with a stiffer right side deformed asymmetrically, undergoing a larger deformation along its left side $\Delta_l > \Delta_r$. In the bottom panels of **Fig. 7C** we show snapshots of the

magnitude of the velocity and of the streamlines during one period for an asymmetric biobot. The streamlines at t = 0.5 s and t = 0.75 s indicate that the biobot is moving from the right to the left (right side of the skeleton corresponding to the stiffer side), which is in agreement with what observed in the experiments. This finding is confirmed in **Fig. 7D** where the velocity of an asymmetric biobot is shown to be negative, i.e. from the right to the left, during the entire period. The average speed of the asymmetric biobot over one period is compared to the symmetric one in **Fig. 7E**, confirming our hypothesis that an asymmetric deformation of the biobot is necessary for its locomotion.
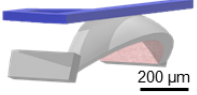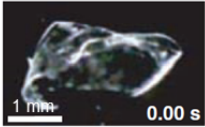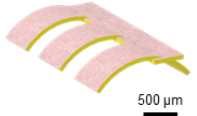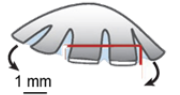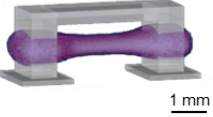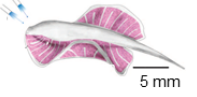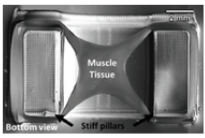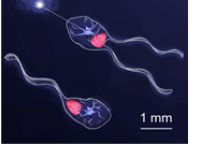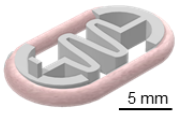
Bio-robot/ Mechanism	Size [mm]	Speed [mm/min]	Body length/min	Schematic
Cardiomyocytes cells assembled to a MEMS system *(17)* Swimming	0.612	2.28	3.72	200 µm
Spatially ordered **cardiomyocytes** on PDMS thin films *(18)* Swimming	6	20	3.33	1 mm 0.00 s
Cardiomyocytes seeded onto a PDMS thin layer consisting of 3 strips *(19)* *Walking*	2	6	3	500 µm
Cardiomyocytes cell monolayer onto flexible elastomer *(31)* Swimming	6	71.53	11.9	1 mm
Cardiomyocytes seeded on a PDMS cantilever structure *(20)* *Walking*	7	14.16	2	1 mm
3D-printed **skeletal muscle**-based hydrogel assembled to flexible asymmetric skeleton *(44)* *Crawling*	5.5	9.36	1.5	1 mm
Cardiomyocytes patterned onto elastomeric ray-like structure *(30)* Swimming	14	90	6.42	5 mm
Computational design of 3D-printed **skeletal muscle**-based hydrogel with tissue bridging the pillars from the skeleton *(49)* *Crawling*	13.6	30	2.20	
Free-standing soft scaffold assembled to **skeletal muscle** tissue and on-board neuromuscular units *(53)* Swimming	3	0.042	0.014	1 mm
Skeletal muscle-based tissue assembled to PDMS-based serpentine spring – this work Swimming	12	33.24	2.77	5 mm

Table 1: Chronological summary of bio-hybrid robotic systems development based on cardiac and

muscular cells, indicating their size, real and relative speed (body length/second), and the

corresponding schematic. Size value corresponds to the larger biobot dimension, being the length or the width, depending on each design. Reprinted with permission from ref. 18 (Copyright 2007 AAAS); reprinted with permission from ref. 31 (Copyright 2012 Springer Nature); reprinted with permission from ref. 20 (Copyright 2012 Springer Nature); reprinted with permission from ref. 44 (Copyright 2016 PNAS); reprinted with permission from ref. 30 (Copyright 2016 AAAS); reprinted with permission from ref. 49 (Copyright 2018 Wiley-VCH); reprinted with permission from ref. 53 (Copyright 2019 PNAS).

Discussion

Biological robots based on skeletal muscle tissue are of interest in the soft robotics area due to the inherent properties of natural tissue that are difficult to replicate with artificial actuators. Muscle-based biobots have been proposed not only as tissue models to study muscle development and regeneration (*43*, *72*), or as drug testing platforms in the biomedical field (*73*, *74*), but these actuators are posed as excellent candidates to study the integration of tissue with complex artificial materials to understand or improve motion mechanisms through biomimetic approaches in robotic platforms (*30*, *31*, *34*, *35*). Here, we report a bio-hybrid robot based on skeletal muscle cells that can swim at speeds comparable to their cardiac counterparts (**Table 1**), also taking advantage of the adaptability and control capabilities inherent to skeletal muscle cells. We reported a biological robot based on a flexible serpentine spring design that is optimized through simulations and subsequently 3D printed. The novelty of a compliant spring-like scaffold instead of a stiffer or tethered one lies in the improved differentiation of the tissue through mechanical self-stimulation upon spontaneous contractions, which creates a feedback loop due to the restoring force of the spring. Moreover, the asymmetry from the serpentine spring skeleton allows the structure to move with two different modes: by inertial swimming at the interface or coasting near a bottom surface. Serpentine spring structures are well-known in the microelectromechanical systems (MEMS) field

to create flexible structure by working with microfabrication techniques (*75*, *76*). Although serpentine springs have been implemented in untethered micro-force sensing microrobots to obtain compliant structures (*77*), such structures have not been included before in a soft robotic living system. The design of the serpentine spring was ideal to be printed by additive manufacturing, obtaining a 3D structure of attractive properties from the mechanical point of view, being of great interest for the design of future 3D printed robotic platforms.

The optimization of the designs, based on several features like asymmetry or coil curvature, was performed *via* FEA simulations, which allowed us to find the appropriate geometrical stiffnesses of each case and then experimentally test them. As expected, we found that the addition of an asymmetric feature in one of the sides resulted in a differential compression of the skeleton, which is known to be necessary for efficient motion (*35*). Moreover, force measurements revealed that differentiation in a compliant spring-like skeleton was beneficial when compared to other static tethered skeletons, such as a 2-post system. The muscle tissue under these conditions showed earlier spontaneous contractions and greater increments of force during the differentiation process. We hypothesize that the dynamic compliance of the skeleton, reacting to the compression with a restoring force, provided an additional level of cyclic mechanical stimulation that helped to achieve a better degree of differentiation. In fact, the potential of expanding the use of such skeleton in other muscle-based biobots configurations would represent a novel approach to implement tailored training protocols that do not require for any external stimuli.

Finally, we characterized the motion of two types of bio-hybrid robots: a symmetric swimmer and an asymmetric swimmer. For the former, we found that motion at the air-liquid interface was not possible due to the generated symmetric flow fields, which was supported by hydrodynamic simulations. In contrast, when the symmetric biobots were placed into the culture medium, a buckling behaviour was observed and the swimmer adopted a curved structure that allowed motion at low speeds, although such motion was unreliable, most likely due to interactions

between the generated flow fields and the surface. Asymmetric biobots, however, presented a reliable and consistent motion, as they already displayed buckling when floating in the air-liquid interface. Stimulation with EPS showed high speeds, up to 800 μm/s and motion studies, as well as hydrodynamic simulations, were consistently confirming the hypothesis that inertia plays a key role in the motion mechanism. Future work should aim at understanding the interactions between the skeleton and surfaces, to comprehend the exact parameters governing this type of motion and cooperative behaviour of several biobots. Moreover, the scalability of these biobots could be investigated by comparing the motion of swimmers with different number of coils and exploring other configuration, mainly due to the versatility that 3D bioprinting offers in terms of shape and multi-material 3D printing, as well as studying the implementation of nanocomposites.

In summary, the bio-hybrid swimmer based on skeletal muscle cells hereby reported move at speeds faster than the largest skeletal-muscle-based biobots up to date (*49*) and comparable to other cardiomyocyte-based bio-swimmers (*30*). We use 3D printing of PDMS to fabricate serpentine-like skeletons that can act as a spring when a muscle ring compresses them, resulting in compliant scaffolds that aid in the differentiation of the tissue. The optimization of the designs via FEA simulations allowed us to find the appropriate geometrical stiffnesses by studying their asymmetry and coil curvature. We found that differentiation in a compliant spring-like skeleton was beneficial when compared to other static tethered skeletons due to its associated mechanical self-training capabilities, resulting in earlier spontaneous contractions and greater increments of force during the differentiation process. We hypothesize that the dynamic compliance of the skeleton, reacting to the compression with a restoring force, provides an additional level of cyclic mechanical stimulation that aids to achieve an improved maturation. Also, the hydrodynamics study of the different motion modes provides a fundamental understanding over its motion mechanism, demonstrating the potential of applying this serpentine-like structure to provide asymmetry and achieve enhanced force outputs on future biobots configurations. Such bio-hybrid

compliant actuators can be envisioned as basic units to construct a modular system that allows scaling up the current bio-hybrid robotic systems, not only providing better muscle cells alignment that impacts on the final force output, but obtaining additional degrees of freedom in terms of motion capabilities due to the observed buckling effect (i.e. agonistic-antagonist joint actuator). Further research in the bio-hybrid robotics field should be focused on the integration of several tissues and obtaining more complex, yet useful, ways of actuation that can finally prove the benefits of using native muscle tissue instead of man-made soft actuators. Once achieved, the next main challenges will reside in ensuring long-term stability of the constructs and tolerance to different environments, requiring the implementation of novel and soft bioreactors to protect the tissue and the improvement of the control mechanisms. All these advances will undoubtedly imply a coordinated interdisciplinary effort between different fields of expertise, ranging from 3D bioengineering and biology, to materials science and mechanical engineering.

Materials and Methods

Biobot fabrication

C2C12 mouse myoblasts were purchased from ATCC. Growth medium (GM) consisted of high glucose Dullbecco's Modified Eagle's Medium (DMEM; Gibco®) supplemented with 10% Fetal Bovine Serum (FBS), 200 nM L-Glutamine and 1% Penicillin/Streptomycin. Cells below passage 4 were used before reaching 80% confluency in Corning® T-75 flasks. Differentiation medium (DM) consisted of high glucose DMEM containing 10% Horse Serum (Gibco®), 200 nM L-Glutamine (Gibco®), 1% Penicillin-Streptomycin (Gibco®), 50 ng/ml insulin-like growth factor 1 (IGF-1, Sigma-Aldrich) and 1 mg/ml 6-aminocaproic acid (ACA, Sigma-Aldrich). C2C12 skeletal myoblasts were harvested from the flask when reaching 80% confluency. The mixture adapted from Raman et al. (*42*) (see SI) was manually casted immediately on a 3D-printed PDMS injection

mold. The tissue construct was left in a cell incubator (37 ºC, 5% CO_2) for 30 min, and GM supplemented with ACA to avoid degradation of collagen by proteases was added and kept for 2 days. Then, the tissue was gently lifted from the mold and transferred to either a (i) 3D-printed compliant skeleton or (ii) a 2-post system. Spring like skeletons of different ratios (1:20, 1:15 or 1:10, with or without dye) were cured at 80 °C overnight (78). The designs of the skeletons were done with AutoCAD (v. 2019), exported as .stl files, and transformed into GCode, to be later printed with Cellink's Inkredible+ 3D bioprinter. The 2-post system (3 mm high, 0.5 mm wide and with 2 mm of lateral width) was 3D-printed with PDMS of a 1:20 and crosslinked at 37 °C for several days. Once cell-laden scaffold is transferred to the compliant skeleton, the culture medium was changed to DM supplemented with ACA and IGF-1. After 4 days in DM, the structure is drawn in a plastic petri dish to obtain the desired buckling effect.

Biobot force characterization

The protocol described by Mestre *et al.* (43) for force measurements in a two post-system for muscle-based actuators was adapted to determine the role of the compliant skeleton on the fabricated biobots' final force. The recording of the whole setup undergoing EPS was carried out inside an inverted microscope (DMi8, Leica), in a chamber that allowed to mimic physiological conditions (37 °C and 5% CO_2). For force measurement of the biobots in **Fig. 4**, the tissue was gently transferred at D4 or D14, depending on the experiment, into a 2-post system, and their force measured by deflection of the posts by the cell-laden scaffold. Pulses of different frequencies of 1 ms were applied, keeping a constant voltage of 15 V. Euler–Bernoulli's beam bending equation was used to estimate the forces and stresses exerted against the posts to the tissue during electrical stimulation (43) (more details in SI).

Motion analysis

Motion evaluation of the bio-hybrid robot was performed with a homemade Python tracking

script based on computer vision algorithms that could characterize the motion of the biobots after being recorded with any type of smartphone camera (**Fig. 5**). In brief, the video file of the recorded biobots was loaded into the script and the first frame was prompted for the user to manually select an ROI covering the whole biobot area (**Fig. S5**). Then, an object tracking algorithm based on an online AdaBoost feature selection (*79*) was applied to this ROI through every frame of the video (more details in SI).

Statistical analysis

Experiments from spontaneous contractions and force measurement in **Fig. 4D** were performed for N = 3-6 independent repeats and error bars represent standard error of the mean. Statistical significance is indicated by * with p-value < 0.05 (Student's t-test). Normality was assessed with the Shapiro-Wilk test and equality of variances with the Levene's test. Viability/metabolic activity assays in **Fig. 4F** and RT-qPCR in **Fig. 4G** were performed for N = 3-4 and N = 3 independent repeats, respectively, and error bars represent standard error of the mean. Statistical significance is indicated by * with p-value < 0.05 (Tukey's HSD test for multiple comparison). Before the post-hoc Tukey's HSD test, one-way ANOVA was performed, the normality of the model residuals assessed with the Shapiro-Wilk test and equality of variances with the Levene's test. Motion fittings in **Fig. 5C** and **Fig. 6D** were performed with the least squares fitting method to a linear equation of the form $x = v \cdot t$, from which the speed was extracted. In these plots, the error bars corresponde to the error of the fitting. Violin plots and motion yield values of Fig. 6B come from N = 26 asymmetric and N = 15 symmetric biobots. Data in tabulated form and a more thorough description of the statistical analysis is available in the Supplementary Materials.

Supplementary Material

Fig. S1. Movement index from the spontaneous contraction evaluation.

Fig. S2. Immunostaining studies by confocal microscopy.

Fig. S3. Myotube diameter study.

Fig. S4. Electrical pulse stimulation (EPS) setup

Fig. S5. Home-made script for tracking of biobots.

Movie S1. Spontaneous contraction evaluation.

Movie S2: Force evaluation between the 2-post system and the spring-like biobot.

Movie S3: Spring-like symmetric biobot actuated at the air-liquid interface (control).

Movie S4: Spring-like symmetric biobot at the bottom surface actuated at different frequencies.

Movie S5: Spring-like asymmetric biobot at the air-liquid interface actuated at different

frequencies.

Data from all figures included in tabular form

References and Notes

1. S. Camazine, J. L. Deneubourg, N. R. Franks, J. Sneyd, E. Bonabeau, G. Theraula, *Self-organization in Biological Systems* (Princeton University Press, 2003), *Princeton Studies in Complexity*.
2. P. Egan, R. Sinko, P. R. Leduc, S. Keten, The role of mechanics in biological and bio-inspired systems. *Nature Communications*. **6**, 7418 (2015).
3. In *Self-Healing Composites* (John Wiley & Sons Ltd, Chichester, United Kingdom, 2014), pp. 21–34.
4. D. B. Dusenbery, Spatial sensing of stimulus gradients can be superior to temporal sensing for free-swimming bacteria. *Biophysical Journal*. **74**, 2272–2277 (1998).
5. L. Ricotti, A. Menciassi, Bio-hybrid muscle cell-based actuators. *Biomedical Microdevices*. **14**, 987–998 (2012).
6. T. Patino, R. Mestre, S. Sánchez, Miniaturized soft bio-hybrid robotics: a step forward into healthcare applications. *Lab on a Chip*. **16**, 3626–3630 (2016).
7. M. Cianchetti, C. Laschi, A. Menciassi, P. Dario, Biomedical applications of soft robotics. *Nature Reviews Materials*. **3**, 143–153 (2018).
8. L. Ricotti, B. Trimmer, A. W. Feinberg, R. Raman, K. K. Parker, R. Bashir, M. Sitti, S. Martel, P. Dario, A. Menciassi, Biohybrid actuators for robotics: A review of devices actuated by living cells. *Science Robotics*. **2**, 1–18 (2017).
9. M. Wehner, R. L. Truby, D. J. Fitzgerald, B. Mosadegh, G. M. Whitesides, J. A. Lewis, R. J. Wood, An integrated design and fabrication strategy for entirely soft, autonomous robots. *Nature*. **536**, 451–455 (2016).
10. R. F. Shepherd, F. Ilievski, W. Choi, S. a. Morin, A. A. Stokes, A. D. Mazzeo, X. Chen, M. Wang, G. M. Whitesides, Multigait soft robot. *Proceedings of the National Academy of Sciences*. **108**, 20400–20403 (2011).

11.   M. T. Tolley, R. F. Shepherd, B. Mosadegh, K. C. Galloway, M. Wehner, M. Karpelson, R. J. Wood, G. M. Whitesides, A Resilient, Untethered Soft Robot. *Soft Robotics*. **1**, 213–223 (2014).

12.   R. V. Martinez, J. L. Branch, C. R. Fish, L. Jin, R. F. Shepherd, R. M. D. Nunes, Z. Suo, G. M. Whitesides, Robotic tentacles with three-dimensional mobility based on flexible elastomers. *Advanced Materials*. **25**, 205–212 (2013).

13.   G. K. Klute, J. M. Czerniecki, B. Hannaford, Artificial Muscles: Actuators for Biorobotic Systems. *The International Journal of Robotics Research*. **21**, 295–309 (2002).

14.   R. H. Baughman, Playing Nature's Game with Artificial Muscles. *Science*. **308**, 63–65 (2005).

15.   C. Appiah, C. Arndt, K. Siemsen, A. Heitmann, A. Staubitz, C. Selhuber-Unkel, Living Materials Herald a New Era in Soft Robotics. *Advanced Materials*. **31**, 1807747 (2019).

16.   L. Sun, Y. Yu, Z. Chen, F. Bian, F. Ye, L. Sun, Y. Zhao, Biohybrid robotics with living cell actuation. *Chemical Society Reviews*. **49**, 4043–4069 (2020).

17.   J. Xi, J. J. Schmidt, C. D. Montemagno, Self-assembled microdevices driven by muscle. *Nature Materials*. **4**, 180–184 (2005).

18.   A. W. Feinberg, A. Feigel, S. S. Shevkoplyas, S. Sheehy, G. M. Whitesides, K. K. Parker, Muscular thin films for building actuators and powering devices. *Science*. **317**, 1366–1370 (2007).

19.   J. Kim, J. Park, S. Yang, J. Baek, B. Kim, S. H. Lee, E.-S. Yoon, K. Chun, S. Park, Establishment of a fabrication method for a long-term actuated hybrid cell robot. *Lab on a Chip*. **7**, 1504-1508 (2007).

20.   V. Chan, K. Park, M. B. Collens, H. Kong, T. A. Saif, R. Bashir, Development of miniaturized walking biological machines. *Scientific Reports*. **2**, 857 (2012).

21.   V. Hosseini, S. Ahadian, S. Ostrovidov, G. Camci-Unal, S. Chen, H. Kaji, M. Ramalingam, A. Khademhosseini, Engineered Contractile Skeletal Muscle Tissue on a Microgrooved Methacrylated Gelatin Substrate. *Tissue Engineering Part A*. **18**, 2453–2465 (2012).

22.   S. R. Shin, C. Shin, A. Memic, S. Shadmehr, M. Miscuglio, H. Y. Jung, S. M. Jung, H. Bae, A. Khademhosseini, X. S. Tang, M. R. Dokmeci, Aligned Carbon Nanotube-Based Flexible Gel Substrates for Engineering Biohybrid Tissue Actuators. *Advanced Functional Materials*. **25**, 4486–4495 (2015).

23.   T. H. Kim, C. H. Kwon, C. Lee, J. An, T. T. T. Phuong, S. H. Park, M. D. Lima, R. H. Baughman, T. M. Kang, S. J. Kim, Bio-inspired Hybrid Carbon Nanotube Muscles. *Scientific Reports*. **6**, 26687 (2016).

24.   L. Ricotti, T. Fujie, Thin polymeric films for building biohybrid microrobots. *Bioinspiration & Biomimetics*. **12**, 021001 (2017).

25.   B. Xu, X. Han, Y. Hu, Y. Luo, C. Chen, Z. Chen, P. Shi, A Remotely Controlled Transformable Soft Robot Based on Engineered Cardiac Tissue Construct. *Small*. **15**, 1900006 (2019).

26.   A. Hasebe, Y. Suematsu, S. Takeoka, T. Mazzocchi, L. Vannozzi, L. Ricotti, T. Fujie, Biohybrid Actuators Based on Skeletal Muscle-Powered Microgrooved Ultrathin Films Consisting of Poly(styrene- block -butadiene- block -styrene). *ACS Biomaterials Science & Engineering*. **5**, 5734–5743 (2019).

27.   L. Vannozzi, T. Mazzocchi, A. Hasebe, S. Takeoka, T. Fujie, L. Ricotti, A Coupled FEM-SPH Modeling Technique to Investigate the Contractility of Biohybrid Thin Films. *Advanced Biosystems*. **4**, 1900306 (2020).

28. R. Takemura, T. Hoshino, Y. Akiyama, K. Morishima, in *2010 International Symposium on Micro-NanoMechatronics and Human Science* (IEEE, 2010), pp. 485-490.

29. M. T. Holley, N. Nagarajan, C. Danielson, P. Zorlutuna, K. Park, Development and characterization of muscle-based actuators for self-stabilizing swimming biorobots. *Lab on a Chip*. **16**, 3473–3484 (2016).

30. S.-J. Park, M. Gazzola, K. S. Park, S. Park, V. di Santo, E. L. Blevins, J. U. Lind, P. H. Campbell, S. Dauth, A. K. Capulli, F. S. Pasqualini, S. Ahn, A. Cho, H. Yuan, B. M. Maoz, R. Vijaykumar, J.-W. Choi, K. Deisseroth, G. v. Lauder, L. Mahadevan, K. K. Parker, Phototactic guidance of a tissue-engineered soft-robotic ray. *Science*. **353**, 158–162 (2016).

31. J. C. Nawroth, H. Lee, A. W. Feinberg, C. M. Ripplinger, M. L. McCain, A. Grosberg, J. O. Dabiri, K. K. Parker, A tissue-engineered jellyfish with biomimetic propulsion. *Nature biotechnology*. **30**, 792–7 (2012).

32. T. J. Wallin, J. Pikul, R. F. Shepherd, 3D printing of soft robotic systems. *Nature Reviews Materials*. **3**, 84–100 (2018).

33. N. di Marzio, D. Eglin, T. Serra, L. Moroni, Bio-Fabrication: Convergence of 3D Bioprinting and Nano-Biomaterials in Tissue Engineering and Regenerative Medicine. *Frontiers in Bioengineering and Biotechnology*. **8** (2020), 326.

34. Y. Morimoto, H. Onoe, S. Takeuchi, Biohybrid robot powered by an antagonistic pair of skeletal muscle tissues. *Science Robotics*. **3**, eaat4440 (2018).

35. C. Cvetkovic, R. Raman, V. Chan, B. J. Williams, M. Tolish, P. Bajaj, M. S. Sakar, H. H. Asada, M. T. A. Saif, R. Bashir, Three-dimensionally printed biological machines powered by skeletal muscle. *Proceedings of the National Academy of Sciences of the United States of America*. **111**, 10125–30 (2014).

36. M. S. Sakar, D. Neal, T. Boudou, M. A. Borochin, Y. Li, R. Weiss, R. D. Kamm, C. S. Chen, H. H. Asada, Formation and optogenetic control of engineered 3D skeletal muscle bioactuators. *Lab on a Chip*. **12**, 4976 (2012).

37. M. Das, K. Wilson, P. Molnar, J. J. Hickman, Differentiation of skeletal muscle and integration of myotubes with silicon microstructures using serum-free medium and a synthetic silane substrate. *Nature Protocols*. **2**, 1795–1801 (2007).

38. K. Shimizu, H. Sasaki, H. Hida, H. Fujita, K. Obinata, M. Shikida, E. Nagamori, Assembly of skeletal muscle cells on a Si-MEMS device and their generative force measurement. *Biomedical Microdevices*. **12**, 247–252 (2010).

39. T. Boudou, W. R. Legant, A. Mu, M. A. Borochin, N. Thavandiran, M. Radisic, P. W. Zandstra, J. A. Epstein, K. B. Margulies, C. S. Chen, A Microfabricated Platform to Measure and Manipulate the Mechanics of Engineered Cardiac Microtissues. *Tissue Engineering Part A*. **18**, 910–919 (2012).

40. T. Hoshino, K. Morishima, Muscle-powered Cantilever for Microtweezers with an Artificial Micro Skeleton and Rat Primary Myotubes. *Journal of Biomechanical Science and Engineering*. **5**, 245–251 (2010).

41. K. Kabumoto, T. Hoshino, Y. Akiyama, K. Morishima, Voluntary Movement Controlled by the Surface EMG Signal for Tissue-Engineered Skeletal Muscle on a Gripping Tool. *Tissue Engineering Part A*. **19**, 1695–1703 (2013).

42. R. Raman, C. Cvetkovic, R. Bashir, A modular approach to the design, fabrication, and characterization of muscle-powered biological machines. *Nature Protocols*. **12**, 519–533 (2017).

43. R. Mestre, T. Patiño, X. Barceló, S. Anand, A. Pérez-Jiménez, S. Sánchez, Force Modulation and Adaptability of 3D-Bioprinted Biological Actuators Based on Skeletal Muscle Tissue. *Advanced Materials Technologies*. **4**, 1800631 (2018).

44. R. Raman, C. Cvetkovic, S. G. M. Uzel, R. J. Platt, P. Sengupta, R. D. Kamm, Optogenetic skeletal muscle-powered adaptive biological machines. *Proceedings of the National Academy of Sciences of the United States of America*. **113**, 3497–3502 (2016).

45. R. Raman, R. Bashir, Biomimicry, Biofabrication, and Biohybrid Systems: The Emergence and Evolution of Biological Design. *Advanced Healthcare Materials* **6**, 1700496 (2017).

46. C. Cvetkovic, M. H. Rich, R. Raman, H. Kong, R. Bashir, A 3D-printed platform for modular neuromuscular motor units. *Microsystems & Nanoengineering*. **3**, 17015 (2017).

47. C. Cvetkovic, M. C. Ferrall-Fairbanks, E. Ko, L. Grant, H. Kong, M. O. Platt, R. Bashir, Investigating the Life Expectancy and Proteolytic Degradation of Engineered Skeletal Muscle Biological Machines. *Scientific Reports*. **7**, 3775 (2017).

48. L. Grant, R. Raman, C. Cvetkovic, M. C. Ferrall-Fairbanks, G. J. Pagan-Diaz, P. Hadley, E. Ko, M. O. Platt, R. Bashir, Long-Term Cryopreservation and Revival of Tissue-Engineered Skeletal Muscle. *Tissue Engineering Part A*. **25**, 1023–1036 (2019).

49. G. J. Pagan-Diaz, X. Zhang, L. Grant, Y. Kim, O. Aydin, C. Cvetkovic, E. Ko, E. Solomon, J. Hollis, H. Kong, T. Saif, M. Gazzola, R. Bashir, Simulation and Fabrication of Stronger, Larger, and Faster Walking Biohybrid Machines. *Advanced Functional Materials*. **28**, 1801145 (2018).

50. Y. Kim, G. Pagan-Diaz, L. Gapinske, Y. Kim, J. Suh, E. Solomon, J. F. Harris, S. Nam, R. Bashir, Integration of Graphene Electrodes with 3D Skeletal Muscle Tissue Models. *Advanced Healthcare Materials*. **9**, 1901137 (2020).

51. O. Aydin, A. P. Passaro, M. Elhebeary, G. J. Pagan-Diaz, A. Fan, S. Nuethong, R. Bashir, S. L. Stice, M. T. A. Saif, Development of 3D neuromuscular bioactuators. *APL Bioengineering*. **4**, 016107 (2020).

52. C. D. Kaufman, S. C. Liu, C. Cvetkovic, C. A. Lee, G. Naseri Kouzehgarani, R. Gillette, R. Bashir, M. U. Gillette, Emergence of functional neuromuscular junctions in an engineered, multicellular spinal cord-muscle bioactuator. *APL Bioengineering*. **4**, 026104 (2020).

53. O. Aydin, X. Zhang, S. Nuethong, G. J. Pagan-Diaz, R. Bashir, M. Gazzola, M. T. A. Saif, Neuromuscular actuation of biohybrid motile bots. *Proceedings of the National Academy of Sciences*. **116**, 19841–19847 (2019).

54. S. Hinds, W. Bian, R. G. Dennis, N. Bursac, The role of extracellular matrix composition in structure and function of bioengineered skeletal muscle. *Biomaterials*. **32**, 3575–3583 (2011).

55. S. Wu, Q. Ze, R. Zhang, N. Hu, Y. Cheng, F. Yang, R. Zhao, Symmetry-Breaking Actuation Mechanism for Soft Robotics and Active Metamaterials. *ACS Applied Materials and Interfaces*. **11**, 41649–41658 (2019).

56. C. A. Powell, B. L. Smiley, J. Mills, H. H. Vandenburgh, Mechanical stimulation improves tissue-engineered human skeletal muscle. *American Journal of Physiology-Cell Physiology*. **283**, 1557–1565 (2002).

57. D. G. Moon, G. Christ, J. D. Stitzel, A. Atala, J. J. Yoo, Cyclic Mechanical Preconditioning Improves Engineered Muscle Contraction. *Tissue Engineering Part A*. **14**, 473–482 (2008).

58. A. J. Engler, M. A. Griffin, S. Sen, C. G. Bönnemann, H. L. Sweeney, D. E. Discher, Myotubes differentiate optimally on substrates with tissue-like stiffness. *The Journal of Cell Biology*. **166**, 877–887 (2004).

59. R. Mestre, T. Patiño, M. Guix, X. Barceló, S. Sanchez, Design, Optimization and Characterization of Bio-Hybrid Actuators Based on 3D-Bioprinted Skeletal Muscle Tissue, in *Biomimetic and Biohybrid Systems. Living Machines 2019. Lecture Notes in Computer Science* (Springer-Verlag, 2018), pp. 316–320.

60. D. M. Brown, T. Parr, J. M. Brameld, Myosin heavy chain mRNA isoforms are expressed in two distinct cohorts during C2C12 myogenesis. *Journal of Muscle Research and Cell Motility*. **32**, 383–390 (2012).

61. U. K. Muller, J. L. van Leeuwen, Swimming of larval zebrafish: ontogeny of body waves and implications for locomotory development. *Journal of Experimental Biology*. **207**, 853–868 (2004).

62. V. Mwaffo, S. Butail, M. Porfiri, In-silico experiments of zebrafish behaviour: modeling swimming in three dimensions. *Scientific Reports*. **7**, 39877 (2017).

63. A. P. Berke, L. Turner, H. C. Berg, E. Lauga, Hydrodynamic Attraction of Swimming Microorganisms by Surfaces. *Physical Review Letters*. **101**, 038102 (2008).

64. J. Simmchen, J. Katuri, W. E. Uspal, M. N. Popescu, M. Tasinkevych, S. Sánchez, Topographical pathways guide chemical microswimmers. *Nature Communications*. **7**, 10598 (2016).

65. G. Kokot, A. Snezhko, Manipulation of emergent vortices in swarms of magnetic rollers. *Nature Communications*. **9**, 2344 (2018).

66. G. Vizsnyiczai, G. Frangipane, S. Bianchi, F. Saglimbeni, D. Dell'Arciprete, R. di Leonardo, A transition to stable one-dimensional swimming enhances E. coli motility through narrow channels. *Nature Communications*. **11**, 2340 (2020).

67. E. M. Purcell, Life at Low Reynolds Number. *American Journal of Physics*. **45**, 3–11 (1977).

68. E. Lauga, T. R. Powers, The hydrodynamics of swimming microorganisms. *Reports on Progress in Physics*. **72**, 96601 (2009).

69. L. Turner, W. S. Ryu, H. C. Berg, Real-Time Imaging of Fluorescent Flagellar Filaments. *Journal of Bacteriology*. **182**, 2793–2801 (2000).

70. A. Ghosh, P. Fischer, Controlled propulsion of artificial magnetic nanostructured propellers. *Nano letters*. **9**, 2243–5 (2009).

71. B. J. Williams, S. v Anand, J. Rajagopalan, M. T. a Saif, A self-propelled biohybrid swimmer at low Reynolds number. *Nature communications*. **5**, 1–8 (2014).

72. R. Raman, L. Grant, Y. Seo, C. Cvetkovic, M. Gapinske, A. Palasz, H. Dabbous, H. Kong, P. P. Pinera, R. Bashir, Damage, Healing, and Remodeling in Optogenetic Skeletal Muscle Bioactuators. *Advanced Healthcare Materials*. **6**, 1700030 (2017).

73. H. Vandenburgh, J. Shansky, F. Benesch-Lee, V. Barbata, J. Reid, L. Thorrez, R. Valentini, G. Crawford, Drug-screening platform based on the contractility of tissue-engineered muscle. *Muscle and Nerve*. **37**, 438–447 (2008).

74. R. Mestre, N. García, T. Patiño, M. Guix, M. Valerio-Santiago, N. Almiñana, S. Sánchez, 3D-printed drug testing platform based on a 3D model of aged human skeletal muscle. *bioRxiv* (2020), doi:10.1101/2020.06.18.158659.

75. E. Garcia, N. Lobontiu, Y. Nam, Mechanics of MEMS: a review of modeling, analysis, and design, in *Proceedings of the 2004 SPIE 5390 Smart Structures and Materials,* 26 July 2004, San Diego, CA, pp. 400-409.

76. B. Lips, R. Puers, MEMS Enabled Bendable and Stretchable Silicon Circuits. *Proceedings*. **2**, 837 (2018).

77. W. Jing, S. Chowdhury, M. Guix, J. Wang, Z. An, B. V. Johnson, D. J. Cappelleri, A microforce-sensing mobile microrobot for automated micromanipulation tasks. *IEEE Transactions on Automation Science and Engineering*. **16**, 518–530 (2019).

78. I. D. Johnston, D. K. McCluskey, C. K. L. Tan, M. C. Tracey, Mechanical characterization of bulk Sylgard 184 for microfluidics and microengineering. *Journal of Micromechanics and Microengineering*. **24**, 35017 (2014).

79. H. Grabner, H. Bischof, On-line Boosting and Vision, in *2006 IEEE Computer Society Conference on Computer Vision and Pattern Recognition,* 17-22 June 2006, New York, NY, pp. 260–267.

Author contributions: M.G, R.M and T. P. conceived the study design, performed the experimental work and corresponding data collecting and analysis, and manuscript writing. J. F.

and G.Z. participated in the experimental procedures. The mechanical and hydrodynamical simulations on finite element analysis were conducted by R. M. and M. D. C., respectively. M. D. C. also contributed to the manuscript writing. S.S. participated in the study design, project supervision and manuscript writing.
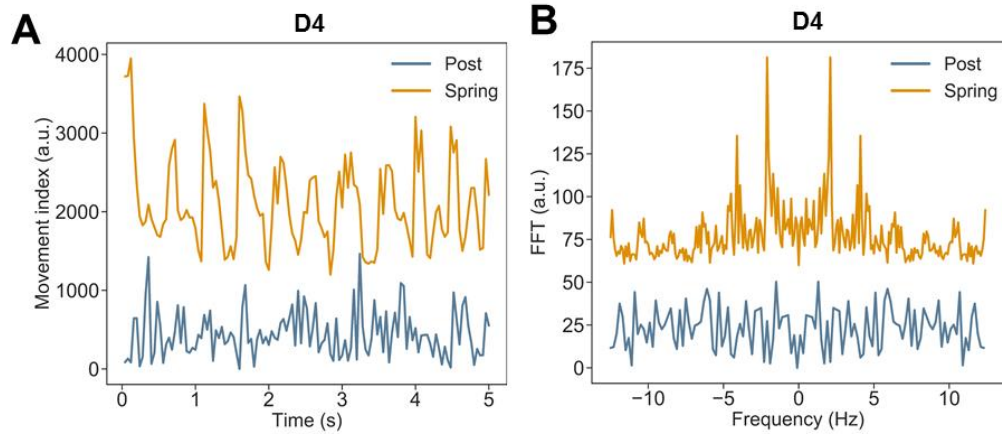
Fig. S1. Movement index (A) and corresponding Fourier transform (B) corresponding to the spontaneous contractions observed at D4.
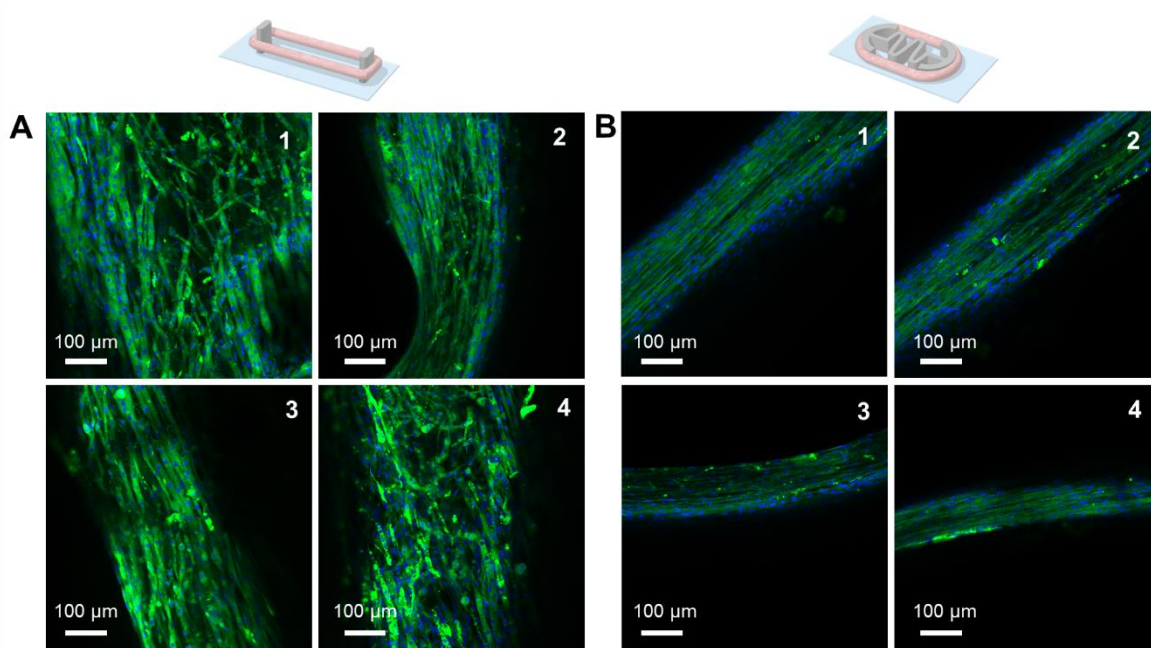
Fig. S2. Confocal microscopy images from immunostaining of samples differentiated in the 2-post system (**A**) or in the spring-like system (**B**), showing the differences in alignment. Green: Myosin Heavy Chain II; blue: cell nuclei (Hoechst).
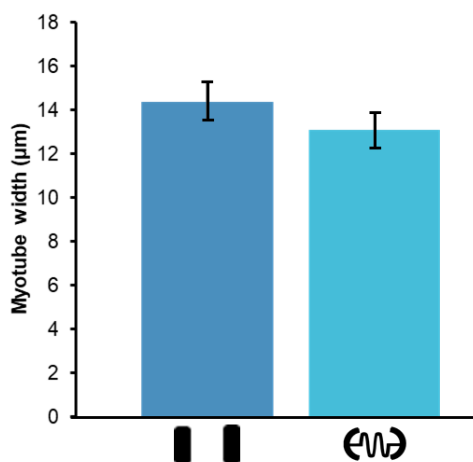
Fig. S3. Myotube diameter for samples differentiated in the two-post system and the spring-like skeleton.
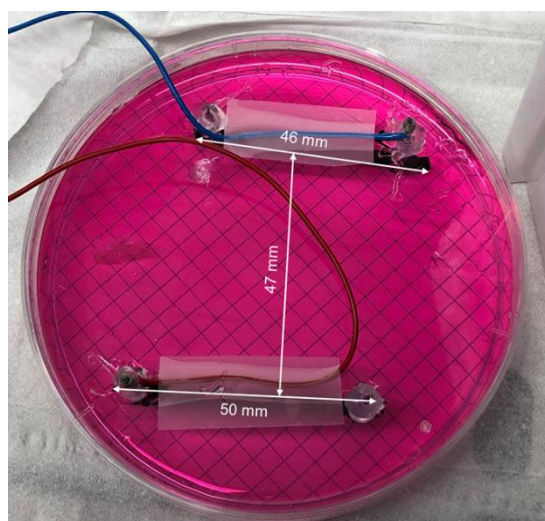
Fig. S4: **Electrical pulse stimulation (EPS) setup**. The setup for EPS was composed by a waveform generator (PM8572, Tabor Electronics), an oscilloscope (DS1104Z, Rigol), a signal amplifier x15, and a set of carbon-based handmade electrodes consisting of two graphite rods (cat. number 30250, Ladd Research) placed on opposite sides of a plastic Petri dish. Both for force measurement and motion evaluation experiments, the recording was carried out inside an inverted microscope (DMi8, Leica) in a chamber that allowed to mimic physiological conditions (37 °C and 5% CO_2). The experiments were run in a plastic petri dish of 8.8 cm diameter, where the electrodes

where coupled after the biobot was moved to the cultures media and conveniently located at the interface or inside the solution. Motion videos of the biobots were recorded with a smartphone, keeping a grid paper below the Petri dish for calibration purposes. Pulses at a different frequency and constant width (1 ms) and voltage (15 V) were applied to study its effect on the biobots motion performance.
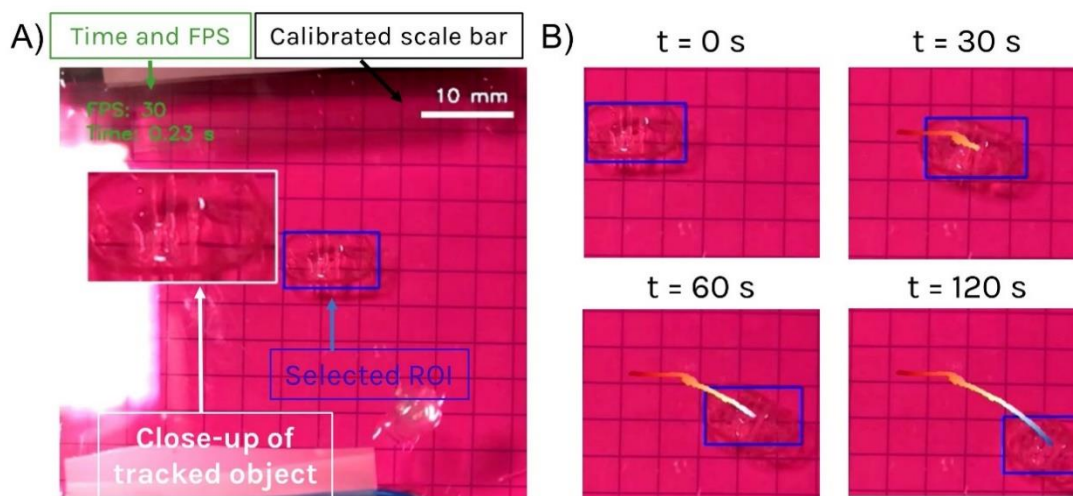
Fig. S5: Home-made script for tracking of bio-bots. (**A**) Snapshot of the initial frame of the tracking, in which several features can be observed: i) the time and FPS of the video are stamped on the top left corner of the video; ii) an ROI is manually selected to contain the biobot, or part of it, which is tracked along the video; iii) the grid paper below the Petri dish is used to calibrate the spatial dimensions; and iv) a close-up of the tracked object inside the ROI is displayed to make sure that the biobot is being properly tracked. (**B**) Snapshots of a tracking, showing a color-coded trajectory, going from red (short time) to blue (long time).

Movies at Supplementary information

Movie S1: Spontaneous contraction evaluation between the 2-post system and the spring-like.

Movie S2: Force evaluation between the 2-post system and the spring-like biobot.

Movie S3: Spring-like symmetric biobot actuated at the air-liquid interface (control).

Movie S4: Spring-like symmetric biobot at the bottom surface actuated at different frequencies.

Movie S5: Spring-like asymmetric biobot at the air-liquid interface actuated at different frequencies.

Extended materials and methods

Cell-laden hydrogel composition

A centrifuged cell pellet with 3 million cells in total was mixed with 54 µL of cold GM supplemented with 1 mg/mL of ACA (Sigma-Aldrich), 12 µL of a stock solution of 50 U/mL of thrombin, 90 µL of Matrigel®. Then, this cell-laden hydrogel was mixed with a stock solution of fibrinogen at 8 mg/mL at a 1:1 ratio, achieving final concentrations of 30% (v/v) Matrigel® and 4 mg/mL fibrinogen.

Immunostaining

Tissue constructs were washed three times in PBS and then fixed with a 3.7% paraformaldehyde in PBS for 15 min at RT, followed by three washes in PBS and stored until use. For immunostaining, cells were permeabilized by 0.2% Triton-X-100 in PBS. After washing thrice in PBS, the constructs were incubated with 5% Bovine Serum Albumin (BSA) in PBS (PBS-BSA) to block unspecific bindings. Then, the tissues were incubated for 2 h at RT and dark conditions with a 1/400 dilution of Alexa Fluor®-488-conjugated Anti-Myosin Heavy Chain II antibody (eBioscience) in 5% PBS-BSA. The unbound antibodies were washed out with PBS, and cell nuclei were stained with 1 µl/mL Hoechst 33342 (Life technologies). Finally, the tissue samples were washed thrice in PBS and stored at 4 °C until their analysis. The fluorescently labelled tissue constructs were imaged under a Zeiss LSM 800 confocal scanning laser microscope (CSLM), with

a diode laser at 488 nm and 405 nm excitation wavelength for Myosin Heavy Chain II and cell nuclei. Alignment analysis was performed with ImageJ ver.1.47q (National Institutes of Health, Bethesda, MD) and the directionality plugin (v. 2.0).

Viability/metabolic activity assay with PrestoBlue™

PrestoBlue™ cell viability reagent was purchased from ThermoFischer (A13262) as used according to the manufacturer's instructions. Briefly, right before replacing differentiation media every 2-3 days, PrestoBlue was added at a 1:10 ratio with respect to the total volume of media in the Petri dish. After 2 h, 10 µL of the media was added to a 96-well plate and measured with a Spark® multimode microplate reader in absorbance mode. The signal at 560 nm was normalized to the signal at 600 nm and the background of only medium controls was subtracted. Three technical replicates were performed for each biological replicate.

RT-qPCR

Total RNA of 3 biological replicates per condition were extracted using the RNeasy mini kit (QIAGEN, 74134) according to manufacturer's instructions. The concentration and purity of the RNA extraction was checked with Nanodrop ND-1000 (Thermo Scientific). A total amount of 500 ng of RNA were converted into cDNA using the ReverAid First Strand cDNA Synthesis Kit (Thermo Scientific, K1622). RT-qPCR reactions were performed with PowerUp SYBR Green Master Mix (Applied Biosystems, A25742), used according to manufacturer's instructions with 500 ng of cDNA and the target primers in a total volue of 10 µL in a StepOnePlus Real-Time PCR System (Applied Biosystems, 4376600). All target genes were normalized to the expression of GAPDH, which was constant for all experiments. Melt-curve tests were carried out to ensure that only one amplicon was being amplified and negative and non-template controls were performed to ensure purity of the samples and reagents. The following primers were used:

- GAPDH: FW (5' ATGGTGAAGGTCGGTGTGAA 3')

  RV (5' GAGGTCAATGAAGGGGTCGT 3')

- Myogenin: FW (5' CCCTACAGACGCCCACAATC 3')

                   RV (5' ACCCAGCCTGACAGACAATC 3')

- MyHCI: FW (5' GCCCCAAGCACAAGGAGT 3')

                   RV (5' AGCCCCAAGAAATAAGGACAG 3')

- MyHCIIa: FW (5' GCAGAGACCGAGAAGGAG 3')

                   RV (5' CTTTCAAGAGGGACACCATC 3')

- MyHCIIb: FW (5' GAAGGAGGGCATTGATTGG 3')

                   RV (5' TGAAGGAGGTGTCTGTCG 3')

- MyHCIIx: FW (5' GCGACAGACACCTCCTTCAAG 3')

                   RV (5' TCCAGCCAGCCAGCGATG 3').

Object tracking algorithm

The bio-bot tracking algorithm was written in Python (v. 3.7) and was based on machine learning through an online AdaBoost feature selection algorithm that was applied to a ROI across every frame of the video. This algorithm extracts identifying features from the object to track its position through time, even if the biobot rotates and changes direction. As smartphone videos can be located at different distances and are not calibrated, the script also allowed manual calibration of the video by using a calibrated grid paper as background. Before starting the tracking, the user could manually draw a line along one of the squares and the script would find the conversion pixel/mm to calibrate the displacements and create a scale bar at the top of the image. Moreover, time in seconds and frames per second (FPS) of the original video were displayed on top, as well as a close-up image of the tracked object online, to ensure that the tracking was capturing the bio-bot properly during the video. The central position of the ROI in mm was stored and used to generate a color-coded trajectory on the images (**Fig. S2**), as well as to plot the total displacement and compute the speed of motion.

Biobots Reynolds number regime

The Reynolds number (Re) allows to differentiate between regimes of motion in which laminar flows (typical of viscous motion) or turbulent flows (typical of inertial motion) are dominant. The Re number is defined as $Re = {v\,L}/{v}$, where v is the characteristic fluid velocity, L is the characteristic length of the swimmer and v the kinematic viscosity of the fluid. In our case, given an approximated size of 10 cm and speeds of the biobots between 100-500 µm/s, we find Re numbers of the order of 1-5. In this range, both viscosity and inertia play a significant role.

Data acquisition for the force characterization studies

In order to evaluate the force from the cell-laden scaffold within the biobot, it was required to firstly obtain z-stack images of the posts to calculate the exact height of the tissue. The displacement of the posts upon contractions was calculated with a homemade Python script that obtained the displacement in pixels along a line perpendicular to the post border. This distance was translated into micrometers. The equation $P = \dfrac{3EI_z\, y(a)}{a^3}$ was used, where P is the applied force, E is the Young's modulus, I_z is the second moment of area of the post around the z axis, a is the height at which the tissue is pulling from the post and $y(a)$ is the displacement of the post at that height, was used to determine the force exerted.

Mechanical deformation simulations

Optimal geometrical parameters on the compliant skeleton were evaluated by using finite element analysis (FEA). By performing a force sweep in the range of 10-100 µN (symmetrically at both edges), based on previous reports (*26, 34*), we can simulate a compression of the skeleton in the same way as the tissue would do. The maximum compression of the complaint skeleton was plotted in terms of the force (**Fig. 3**), revealing a linear elastic response dictated by Hooke's law, that allowed us to calculate the geometrical stiffness of the material, k, by the equation $F = kx$,

where F is the applied force and x the compression. With small forces in the range of hundreds of µN, the yield criterion of the von Mises stress is not fulfilled, as the maximum stress is much lower than the yield stress of PDMS (71). Therefore, a linear analysis is appropriate to model the deformations of the material.

Simulations of mechanical deformation in 3D were performed using the .stl files of the designs generated by AutoCAD. The equilibrium equations for solid mechanics given by Newton's second law were solved:

$$\rho \frac{\partial^2 \boldsymbol{u}}{\partial t^2} = \boldsymbol{\nabla} \cdot \boldsymbol{S}$$

where ρ is the density of the material, $\boldsymbol{u}$ is the displacement vector and $\boldsymbol{S}$ is the second Piola-Kirchhoff stress tensor. The Young's modulus of the material was set to $E = 255$ kPa and the poisson ratio to $v = 0.495$, as PDMS is nearly incompressible. Two point loads following the dynamics of a single twitch contraction, measured experimentally, were applied on both sides of the skeleton in the x axis, normalized with a maximum value in the range 10-100 µN. These boundary loads model the contraction force applied by the tissue. The material was assumed to be isotropic and linear, due to the small forces and deformations that yielded von Mises stresses that were well below the yield stress of PDMS. The von Mises stress is used to predict yielding of materials under complex loading from the results obtained from uniaxial tensile test. They represent the equivalent stress across the structure and provide useful information about their distribution along the whole structure. These time-dependent equations were solved for the approximate duration of a contraction (t = 0:5 s) using the finite element method. The volume of the skeleton was meshed with tetrahedral elements and a MUMPs solver was used. To obtain the compression vs force relationship, the maximum displacement along the x-axis, which coincided with the time of maximum force, was computed for the left side, $x_l = \max(u_{x,l})$, and the right side, $x_r = \max(u_{x,r})$ and plotted in terms of the force. A linear least-squares fitting to the equation

$x = k^{-1}F$, allowed us to obtain the inverse of the geometrical stiffness, k^{-1}, for each side of the skeleton.

Biobot kinematic model

Hydrodynamics simulations were performed to demonstrate that symmetric spring-like skeletons should produce no net motion upon muscle contractions. Due to the high computational power of simulating the deformation of three-dimensional structures coupled with hydrodynamics, a 2D model was used instead (**Fig. 5C**). The flow fields of an incompressible liquid surrounding the symmetric design, governed by the Navier-Stokes equations, were numerically computed by FEA simulations considering the deformations that the tissue contractions apply on the skeleton. Since the deformations along the scaffold are small and can be considered linear (**Fig. 3**), the boundary conditions could be applied directly in the undeformed shape of the skeleton, thus avoiding mesh deformations and greatly reducing computational time. The contractions of the tissue were approximated by a continuous function, $g(t)$, that closely followed the shape an actual contraction profile (with a fast increase and a lower relaxation) to ensure derivability of the function. At both the left and right side of the skeleton, the deformations were defined as $d_l(t) = \Delta_l \, g(t)$ and $d_r(t) = \Delta_r \, g(t)$, respectively, where Δ_l and Δ_r were the deformations achieved at the state of maximum compression for left and right size, respectively. In this case, due to the symmetry of the design, $\Delta_l = \Delta_r$. These two values were obtained from the previous mechanical simulations of the skeleton (Figure 1.3), assuming a force of 100 µN, the same order of magnitude of the forces measured in Figure 1.4. On the rest of the biobot, namely the spring section, the deformation was approximated by a function $d(t)$, which varied linearly between $d_l(t)$ and $d_r(t)$, a characteristic that was also demonstrated by mechanical simulations. Finally, the x-component of the fluid flow on the biobot boundary was computed as the derivative of the deformation, $v_x(t) = \frac{d \, d(t)}{dt}$.

In more detail, as shown in **Fig. 7**, the computational domain was a square of side L from which the section of the biobot was carved out. We considered a cartesian coordinate system that fixed to the centre of the biobot. The motion of the incompressible liquid surrounding the biobot was governed by the Navier-Stokes equations:

$$\rho \frac{\partial \boldsymbol{v}}{\partial t} + \rho \boldsymbol{v} \cdot \nabla \boldsymbol{v} = \eta \nabla^2 \boldsymbol{v} - \nabla p$$

$$\nabla \cdot \boldsymbol{v} = 0$$

$$(1.1)$$

where $\rho = 1000 \text{ kg/m}^3$ is the density of the liquid and $\eta = 10^{-3}$ Pa·s its shear viscosity. The motion of the biobot is driven by the shape deformations of the PDMS skeleton generated by the muscle tissue. These deformations generate fluid flows, which then drive the motion of the biobot. Experiments and finite elements simulations (**Fig. 3**) showed that the shape deformations were small and therefore we could apply the boundary conditions directly at its undeformed shape. This assumption greatly simplified the simulations, since mesh deformation could be avoided.

Numerical simulations of the deformation of the biobot showed that the deformation was concentrated in the spring part of the skeleton. Under the load applied by the tissue, the two curved parts on either side of the biobot were displaced as a rigid body with the deformation being concentrated in the spring. We used this finding to assume that the two curved sides were displaced as a function of time along the *x*-axis. We then assumed that the displacement varied linearly along the skeleton. The deformation on the left side was given by $d_l(t) = \Delta_l \, g(t)$ and on the right side it was given by $d_r(t) = \Delta_r \, g(t)$, where Δ_l and Δ_r are the amplitudes of the displacement of the left and of the right part of the biobot. Experimentally Δ_l and Δ_r could be different if the skeleton has a left-right asymmetric stiffness (**Fig. 3C**). The deformation on the rest of the biobot was denoted by $d(t)$ and it varied linearly between $d_r(t)$ and $d_l(t)$ along the *x*

coordinate, something that was also demonstrated by previous simulations (see **Fig. 7A** for a schematic representation).

The dimensionless function $g(t)$ determined the time variation of the deformation. To mimic the periodic nature of the loading and relaxation of the muscle cells, we approximated the contraction by $g(t) = e^{3g^*(t)-3}$, where $g^*(t)$ is specified by the nonlinear implicit equation:

$$g^*(t) = \sin[2\pi f\, t + 0.8\, g^*(t)], \qquad (1.2)$$

with f being the frequency of the EPS tissue stimulation. As it is shown in **Fig. 7B**, the normalized displacement prescribed by $g(t)$ closely follows that of measured experiments. The advantage of using $g(t)$ over an interpolation of the experimental data is that $g(t)$ is periodic and the average over one period of its time derivative is zero. The latter property is important to guarantee that the velocity on the boundary of the biobot caused by the deformation was zero when averaged over one period.

We assumed that the fluid velocity at the boundary of the biobot was equal to the velocity due to the deformation. Since the biobot was only deforming along the x coordinate and the deformations were small, we had $v_x(t) = \frac{d\, d_l(t)}{dt}$ on the left curved part, $v_x(t) = \frac{d\, d_r(t)}{dt}$ on the right curved part and $v_x(t) = \frac{d\, d(t)}{dt}$ along the rest of the skeleton. This velocity was generated by the boundary actuation of the biobot. Moreover, as we considered a reference frame that moves with the biobot, the velocity at the edges of the square domain is given by $v_x = -V_x$, where V_x is the instantaneous velocity of the biobot. For simplicity, we assumed that the biobot only moves along the x axis. V_x is an additional unknown that must be computed considering the balance of forces on the biobot:

$$m \frac{d}{dt} V_x = F_{h,x}, \qquad (1.3)$$

where m is the mass of the biobot, which we assume has similar density as that of the liquid, and

$F_{h,x}$ is the hydrodynamic force acting on it in the x direction. $F_{h,x}$ is computed as the integral of the

stress tensor along the contour of the biobot:

$$F_{h,x} = \int_{\partial \Omega_P} \eta [\nabla v + \nabla v^T - p\, I] : n\, e_x, \qquad (1.4)$$

where n is the vector normal to the boundary of the skeleton and pointing outwards, e_x is

the unit vector along the x axis and the integral runs along the contour of the biobot $\partial \Omega_P$. By

solving Equations 1.1 to 1.4, one finds the velocity field and the pressure field around the biobot

and its velocity along the x axis. The equations are nonlinear because of the convective term in the

Equation 1.1. We solved these equations using the finite element method. We divided the

computational domain in triangular elements, with more elements near the biobot. We considered a

quadratic interpolation of the velocity field and a linear interpolation for the pressure field. We

used a second order implicit Runge-Kutta time integration scheme.

Data in tabular form

Figure 4B. Spontaneous contraction evaluation at D4 and D10. Main frequency obtained from

Fast Fourier Transform (FFT).

Frequency of contractions (Hz)			
Post at D4	Spring at D4	Post at D10	Spring at D10
No contractions	2.1	1.0	2.9
No contractions	2.4	4.8	2.9
No contractions	4.4	4.7	2.9
No contractions	2.8	3.4	3.7
		2.8	Contractions but main peak not clear
		Contractions but main peak not	Contractions but main peak not

			clear	clear
Average	∅	**2.93**	**3.3**	**3.3**
SEM	∅	**0.51**	**0.7**	**0.2**

Figure 4D. Force measurement of the 2-post system and biobot system at D4 and D14 of differentiation and force increment.

	Force (µN)			
	Post at D6	**Spring at D6**	**Post at D14**	**Spring at D14**
	25.97	56.54	64.23	230.55
	49.52	64.04	40.65	175.17
	46.29	25.36	102.32	68.80
		36.69	99.74	173.08
Average	**40.6**	**45.7**	**76.8**	**161.9**
STD	**12.8**	**17.8**	**67.5**	**29.7**
SEM	**7.4**	**8.9**	**14.8**	**33.8**

Statistical analysis:

	Post D6 vs Spring D6	**Post D14 vs Spring D14**
H$_0$	No difference in mean force	No difference in mean force
H$_1$	Spring samples exert greater force (force difference greater than 0)	Spring samples exert greater force (force difference greater than 0)
Statistical test	One-tailed t-test	One-tailed t-test
p-value	0.21	0.028
Conclusion	Null hypothesis not rejected (no difference in mean force)	Alternative hypothesis accepted (spring samples exert greater force)
Normality (Shapiro-Wilk test p-value)	0.24 (posts), 0.66 (springs)	0.48 (posts), 0.35 (springs)
Variance equality (Levene test p-value)	0.32	0.54

Performed in Python v. 3.7 with the scipy module (v. 1.2.1).

Normality of the samples and equal variances were assessed with the Shapiro-Wilk test and the Levene's test. All of the p-values where higher than 0.05, therefore failing to reject the null hypotheses that the samples belonged to non-normal distributions and that they had different variances.

	Increment from D6 to D14			
	Post D6	**Post D14**	**Spring D6**	**Spring D14**
Data (previous table)	40.6	76.8	45.7	161.9
Error (STD previous table)	12.8	67.5	17.8	29.7
Ratio	1.89		3.54	
Propagated STD*	0.7		1.6	

*Equation used for propagation of error:

$$\epsilon = \sqrt{\left(\frac{1}{b}\right)^2 \epsilon_a^2 + \left(\frac{a}{b^2}\right)^2 \epsilon_b^2},$$

for an equation of the form $f(a,b) = \frac{a}{b}$, where ϵ_a and ϵ_b are the errors (standard deviation in this case) of the variables a and b (in this case, force exerted at D14 and D6, respectively).

Figure 4F. PrestoBlue viability/metabolic activity assay at several time-points after differentiation.

	Normalized absorbance						
	D0 (M)	**D2 (P)**	**D2 (S)**	**D4 (P)**	**D4 (S)**	**D7 (P)**	**D7 (S)**
	0.264868	0.328478	0.31391	0.347924	0.326269	0.364842	0.343769
	0.2452	0.33373	0.330464	0.344621	0.345612	0.351077	0.343618
	0.245936	0.327849	0.334894	0.349319	0.32999	0.362631	0.37984
	0.260906	0.330436	0.329357				
	0.257736						
Average	**0.254929**	**0.330123**	**0.327156**	**0.347288**	**0.333957**	**0.359516**	**0.355743**
STD	**0.008915**	**0.002645**	**0.009149**	**0.002413**	**0.010263**	**0.007392**	**0.020869**
SEM	**0.001783**	**0.000661**	**0.002287**	**0.000804**	**0.003421**	**0.002464**	**0.006956**

Note: M stands for mold, S for spring skeleton, and P for 2-post system.

Statistical test: One-way ANOVA was performed to assess significant differences, obtaining a *p*-value of $1.35 \cdot 10^{-10}$, therefore confirming the alternative hypothesis. Normality of the model residuals was assessed with the Shapiro-Wilk test, yielding a *p*-value of 0.25. Equality of variance was assessed with a Levene's test, yielding a *p*-value of 0.78. A post-hoc Tukey's HSD multiple comparison test with statistical significance defined as *p*-value < 0.5 was then performed to assess the statistical significance between groups. All tests were performed in Python v. 3.7 with the statsmodels module (v. 0.10.0). H_0: no difference in viability between samples and across days. H_1: difference in viability between samples across days.

Figure 4G. RT-qPCR analysis for samples at several time-points after differentiation.

$2^{-\Delta\Delta C_T}$					
	D0 (M)	**D4 (P)**	**D4 (S)**	**D8 (P)**	**D8 (S)**
Myogenin	1.174354 1.322775 0.643747	0.414254016 0.494844061 0.598799396 0.726034124	0.408143423 0.37667659 0.522959013 0.658476329	0.703445073 0.810891154 1.297705532	0.352081935 0.918636606 0.846103587
Average	**1.006**	**0.558**	**0.49**	**0.94**	**0.71**
SEM	**0.079**	**0.070**	**0.06**	**0.18**	**0.18**
MyHCI	0.706784644 1.137515391 1.243814494	0.109215943 0.268086138 0.146435935 0.245830384	0.082396969 0.083787192 0.088191725 0.138218115	0.157031118 0.286253412 0.444556133	0.283653432 0.51779332 0.329372865
Average	**1.03**	**0.192**	**0.10**	**0.296**	**0.377**
SEM	**0.16**	**0.038**	**0.01**	**0.083**	**0.072**
MyHCIIa	0.991506042 0.909110176	1.704060608 3.019839536	2.591782761 1.72368572	13.89065534 16.10049927	43.4068303 128.8332019

	1.109399883 4.479639049	2.396230126 3.484842897	2.0809722	152.2917141	386.6476552
Average	**1.003**	**2.90**	**2.47**	**61**	**186**
SEM	**0.058**	**0.59**	**0.38**	**46**	**103**
MyHCIIb	0.97063924 1.36727293 0.753506391	0.499993541 1.335988138 0.829454405 1.622038147	0.762011379 0.445270573 0.705624754 1.153884754	1.471064766 1.8873271 5.382067588	1.30090317 3.338792229 2.604218742
Average	**1.03**	**1.07**	**0.77**	**2.9**	**2.41**
SEM	**0.18**	**0.25**	**0.15**	**1.2**	**0.60**
MyHCIIx	0.954386039 1.022603978 1.024633249	1.376471267 2.807355639 1.472229182 3.170666504	1.140414201 0.834639871 1.211015109 1.931440014	2.65118501 4.061983927 13.55619725	2.232098502 6.343485365 7.04547183
Average	**1.000**	**2.21**	**1.28**	**6.8**	**5.2**
SEM	**0.023**	**0.46**	**0.23**	**3.4**	**1.5**

Note: M stands for mold, S for spring skeleton, and P for 2-post system.

Statistical test: One-way ANOVA was performed to assess significant differences for each gene. Normality of the model residuals was assessed with the Shapiro-Wilk test, and equality of variance was assessed with a Levene's test. A post-hoc Tukey's HSD multiple comparison test with statistical significance defined as p-value < 0.5 was then performed to assess the statistical significance between groups. All tests were performed in Python v. 3.7 with the statsmodels module (v. 0.10.0). H_0: no difference in gene expression between samples and across days. H_1: difference in gene expression between samples across days. (Only samples within the same genes were compared). Note: none of the experimental groups showed signs of deviations from the assumptions of equality of variance. However, the experimental groups of MyHCIIa and MyHCIIx showed deviations from the normality of residuals, as expected given the visible variability of the values. Nevertheless, given this variability, no significant differences were observed with the post-hoc test, even though the assumption was violated.

Figure 5C. Speed analysis for the case of the symmetric biobot at different frequencies.

	1 Hz	2 Hz	10 Hz
Speed fitting (µm/s)	131.4	149.1	196.7
Error of the fitting (µm/s)	3.4	2.5	2.0

Fitting performed in Python v. 3.7 with the *curve_fit()* function from the *scipy.optimize* module (v. 1.2.1) following a linear equation of the type $x(t; v, b) = vt + b$, where v is the speed of the biobot, t is the time, b is the intercept and $x(t; v, b)$ is the position of the biobot with respect to time. The error comes from the least-squares fitting error, obtained as the square root of the sum of the diagonal elements of the covariance matrix of fitted parameters, as indicated in the documentation of the *curve_fit()* method.

Figure 6B. Violin plots of the speed of symmetric *vs*. asymmetric biobots, yield of moving biobots with respect to the total sample, and violin plots of the speed of asymmetric biobots for different frequencies.

The following table gathers fitted speeds of different types of biobots (symmetric and asymmetric) whose motion was evaluated at different frequencies for Figure 6B left. Each value corresponds to a different experiment (video recorded), but some of the values might refer to the same biobot evaluated at a different frequency. Over the course of the work, more than 200 biobots were fabricated and evaluated. For the motion evaluation, only a subset of those biobots were selected, considering that they had the same characteristics (in terms of geometry, stiffness, proper viability, etc.).

Fitted speed (µm/s)	
Symmetric	**Asymmetric**
60.57658837114768	19.606187241048122
64.45095389098412	95.46746050994493
63.87603135291431	49.169755129188864
196.6635105931881	532.5498167404232
131.40573052326877	345.4999928280615
149.09706373122856	409.86251448562666
0	200.63422609537952
0	794.4669478364343
0	928.4789267767279
0	11.863742458608776
0	16.474452330655804
0	31.303738398233307
0	38.27423063871971
0	33.08993707098418
0	25.84804897591083
0	24.68560689863972
0	29.011438257244546
0	15.511359183167816
	17.916757308610087
	22.118985900617076
	20.738507134668183
	8.346151137708436
	37.34397391284699
	246.3768141024093
	38.01171936046477
	33.428125972472465
	15.833403392124357
	41.10306743976233
	38.95409345776634
	53.13962160489582
	56.72986011138303
	44.55024320383738
	50.67184542014647
	0
	0
	0
	0
	0
	0
	0
	0
	0

		0
Number of samples	**18**	**43**
Average (all)	**37.00**	**100.63**
STD (all)	62.04	205.13
SEM (all)	14.62	31.28
Average (only moving ones)	**111.01**	**131.12**
STD (only moving ones)	56.80	226.06
SEM (only moving ones)	23.19	39.35

Note: biobots with a speed of 0 μm/s where biobots that were properly contracting but not showing any net motion. This data is presented to account for the total number of biobots evaluated (*N*) and calculate the yield of motion (next table).

The yield of motion was evaluated considering the total number of unique biobots (that is, not counting those evaluated at several frequencies) with respesct to the number of unique biobots that were showing net motion and shown in Figure 6B (inset).

	Symmetric	**Asymmetric**
Total number of biobots	16	26
Biobots moving	4	16
Yield of motion	0.25	0.62

Note: the yield of motion is calculated as:

$$\text{Yield} = \frac{\text{Biobots moving}}{\text{Total biobots}}$$

for each type (symmetric and asymmetric).

The following table gathers the fitted speed of asymmetric biobots only according to the frequency at which they were evaluated for the violin plot of Figure 6B right.

Fitted speed (μm/s)	**Frequency (Hz)**
19.606187	1
95.467461	2
49.169755	5
532.549817	1
345.499993	1
409.862514	2
200.634226	2
794.466948	5
928.478927	2
11.863742	1
16.474452	5
31.303738	2
38.274231	1
33.089937	5
25.848049	1
24.685607	2
29.011438	5
15.511359	1
17.916757	2
22.118986	5
20.738507	1
8.346151	2
37.343974	1

246.376814	2
38.011719	1
33.428126	2
15.833403	1
41.103067	2
38.954093	5
53.139622	1
56.729860	1
44.550243	2
50.671845	5

Figure 6D right. Speed analysis for the case of the symmetric biobot at different frequencies.

	1 Hz	2 Hz	5 Hz
Speed fitting (µm/s)	409.9	682.7	794.47
Error of the fitting (µm/s)	5.2	6.8	1.5

Fitting performed in Python v. 3.7 with the *curve_fit()* function from the *scipy.optimize* module (v. 1.2.1) following a linear equation of the type $x(t; v, b) = vt + b$, where v is the speed of the biobot, t is the time, b is the intercept and $x(t; v, b)$ is the position of the biobot with respect to time. The error comes from the least-squares fitting error, obtained as the square root of the sum of the diagonal elements of the covariance matrix of fitted parameters, as indicated in the documentation of the *curve_fit()* method.